



LUNDS
UNIVERSITET

MASTER'S THESIS

Retrieval of cavity embedded
absorption spectrum for quantum
memory applications

QUANTUM INFORMATION GROUP, LUND UNIVERSITY,
SWEDEN

Author:
Robin EKELUND

Supervisor:
Lars RIPPE

February 24, 2014

Populärvetenskaplig sammanfattning

Inom fältet kvantinformation behandlar man information med hjälp av så kallade kvantmekaniska system, vilket tillför både möjligheter och svårigheter i reella tillämpningar. Ett fundamentalt begrepp är den så kallade *kvantbiten*, eller *qubit* som den brukar omnämnas i engelsk litteratur, vilken är den grundläggande komponenten i vilken kvantinformation hanteras, som en direkt analog till biten i en klassisk dator. En klassisk bit har möjligheten att anta värdet ett eller noll, medan en kvantbit dessutom har möjligheten att anta båda dessa värden *på en och samma gång* i en godtycklig proportion, vilket framstår som obegripligt i förhållande till den klassiska värld som vi upplever.

Denna egenskap erbjuder möjligheten att behandla information på ett fundamentallt annorlunda sätt än vad vi är vana vid. Exempel på tillämpningar är kvantdatorer och kvantkryptografi. Kvantdatorer kan utnyttjas för att lösa problem som för klassiska datorer är helt olösbara inom rimlig tid (t.ex. faktorisering av stora tal). Med kvantkryptografins hjälp kan vi dessutom skapa kommunikationskanaler som erbjuder i det närmaste fullständig säkerhet mot intrång vad gäller avlyssning.

Denna rapporten har behandlat så kallade optiska kvantminnen, vilka har till syfte att lagra kvantinformation i form av *fotoner*, dvs. ljuspartiklar. Utförandet består av att en inkommande foton som innehåller en viss kvantbit, absorberas i ett medium och överför kvantinformationen till exciterade elektroner i lagrade joner av typen sällsynta jordartsmetaller. Kvantbiten ska sedan kunna återskapas genom att en ny foton sänds ut från jonerna, med ett identiskt kvanttillstånd jämfört med den ursprungliga fotonen.

I denna avhandling behandlar vi en viss typ av minnen där de olika specifika jonerna endast absorberar fotoner nära en viss motsvarande frekvens eller energi. På det stora hela ter sig detta i att vi får en fördelning när vi tittar på absorptionen som en funktion av frekvensen, vilket vi benämner som *absorptionsspektrumet*. Genom olika tekniker är det möjligt att i detalj utforma denna fördelning, vilket är avgörande för hur effektivt det optiska kvantminnet i slutändan blir.

Genom att dessutom omgärda det absorberande mediumet med två delvis genomskinliga speglar, är det möjligt att ytterligare förbättra prestandan på minnet (en *kavitet* har introducerats). Denna typ är under utveckling i Lund, och har redan i experiment visat hög potential. Detta komplement tillför dock ytterligare problem i den mån att speglarna döljer absorptionsspektrumet för den utsomstående observatören, till följd att vi förlorar kontroll över minnet och därmed inte kan uppnå minnets fulla kapacitet.

Denna rapport har därför utvecklat en metod eller algoritm med syftet att lösa detta problem. Lösningen ter sig som så att genom att jämföra det elektriska fältet av en inkommande och reflekterad ljuspuls med hjälp av en algoritm, är det möjligt att indirekt klargöra utseendet på det i kaviteten existerande absorptionsspektrumet. I rapporten utvecklades också en simulator med syftet att simulera det elektriska fältet inuti kaviteten, så att den utvecklade metoden kunde testas på den resulterande utdatan. Resultaten kunde bedömas som lovande då avvikelsen mellan det riktiga och det beräknade absorptionsspektrumet kunde sägas vara låg i de fall som undersöktes.

Acknowledgements

My thanks goes out my supervisor Lars Rippe for his counselling and supervision and to Stefan Kröll for his advice and help. The rest of the quantum information group has my thanks and appreciation as well. I would also like to include a special thanks to former master student Axel Thuresson, for the assistance given on his previous work.

Abstract

One of the important building blocks in the quantum information field, is the so called quantum memory. Processing is usually performed on quantum information in the form of qubits, which is an analogy to the classical bits in a normal computer. A big concern however is the fact that quantum information which is represented by some quantum state of one or several particles, is easily destroyed by outside perturbations. Quantum memories which are intended to hold the quantum information, therefore present a major challenge in the real world implementation.

By using rare-earth doped crystals in impedance matched cavities in connection with a scheme based on Atomic Frequency Combs (AFCs), it's possible to create very efficient optical quantum memories. The purpose is to store incoming photons and fully preserve its quantum mechanically described parameters such as phase and polarization.

In Lund such hardware is in development, which has already showed promise with some comparatively high recorded efficiencies. However there are still technical hindrances or difficulties which prevents us from fully making use of this technique.

One these problems include the fact that since a cavity used, the rest of the storage crystal is put into obscurity, in the sense that we have no way of determining how the absorption spectrum appears inside the cavity. The aim of this thesis is to present a possible solution, in the form of some sort of algorithm which can be applied on measurement data.

Such an algorithm has been proposed in this thesis, which uses the reflected and transmitted fields from the cavity, and calculates a hypothetical absorption spectrum in the cavity medium. To determine the efficiency or validity of the method, it was applied on simulated data, originating from both a third-party developed model, and model developed in this thesis. Both of these combine quantum mechanics and Maxwell's equations, to form a set of equations called the Maxwell-Bloch equations.

Contents

1	Introduction	2
1.1	Background	2
1.2	Optical Quantum Memory	3
1.2.1	3-level system	4
1.2.2	Inhomogenous broadening	5
1.2.3	Absorption profile shaping	6
1.2.4	AFC	6
1.2.5	Introducing a cavity	7
1.3	Description of the problem	8
1.4	Aim of this thesis	9
1.5	Solution	9
1.6	Structure	9
2	Theory	11
2.1	Electric field representation	11
2.2	Maxwell equations	13
2.3	Bloch equations	14
2.3.1	Hamiltonian	14
2.3.2	Rabi frequency	15
2.3.3	Schrödinger equation	16
2.3.4	Dipole moment	17
2.3.5	Complete Bloch equation	18
2.4	Cavity	20
2.4.1	Cavity mirrors	20
2.4.2	Cavity modes	22
3	Analysing tool	23
3.1	Introduction	23
3.2	Derivation	24
3.2.1	Mirror interface matching	24
3.2.2	The dispersion model	25
3.2.3	Final formulas	26
3.2.4	Summary and comment on the algorithm	27
3.3	Models for testing	28
3.3.1	Interference model	28
3.3.2	Maxwell-Bloch model	29
3.4	Results	29
3.4.1	Interference model	30

3.4.2	Maxwell-Bloch model	33
3.5	Discussion	34
4	Maxwell-Bloch simulator	39
4.1	Derivation	39
4.1.1	Maxwell-Bloch equations	39
4.2	Discretization	45
4.2.1	Bloch equation	46
4.2.2	Maxwell equation	46
4.3	Result	51
4.3.1	A note on the input field used	51
4.3.2	Relative error	52
4.3.3	Some different cases	53
4.3.4	Noise sensitivity	54
4.4	Discussion	61
5	Experiment	63
6	Summary	66
A	Code	67
A.1	Simulator	67
A.2	Library	67
A.3	Visualization	69

Abbreviations and glossaries

AFC Atomic Frequency Comb. 3, 6, 7, 67

AOM Acousto Optic Modulator. 64, 65

AT Analysing Tool. 9, 23, 26, 30, 32, 39, 54, 62, 66, 69

detuning The frequency difference δ from the laser or central frequency. 11, 15, 17, 52, 68

MB Maxwell-Bloch. 23, 28, 38, 39, 54, 61

OQM Optical Quantum Memory. 3, 5, 9, 23, 64

SNR Signal to Noise Ratio. 54, 57, 60–62

List of Figures

1.1	3-level energy diagram	4
1.2	Illustration and graph of the inhomogenous broadening in a crystal lattice.	5
1.3	A principal absorption profile	7
1.4	Crystal cavity with an unknown inside absorption spectrum	8
1.5	Suggested method for validating the method.	10
2.1	Field propagation inside the cavity	13
2.2	Illustration of the Bloch sphere	15
2.3	Cavity crystal, with outside and inside fields displayed	20
3.1	Transmission and reflection spectra in the GHz range, using an interference simulator.	30
3.2	Transmission and reflection spectra in the GHz range, using an interference model with an absorbing media.	31
3.3	Real values refractive index spectrum, using an interference model with an absorbing media.	32
3.4	Transmission and reflection spectra, using an interference model with an absorbing media.	32
3.5	Absorption spectrum, including the computed profiles and the original for comparison.	33
3.6	Transmission and reflection spectra. Case 1, with medium cavity detuning	34
3.7	Transmission and reflection spectra, Case 2, with a small cavity detuning	35
3.8	Transmission and reflection spectra. Case 3, with no cavity detuning	36
3.9	Transmission and reflection spectra. Case 3, with no cavity detuning	37
3.10	Field intensities of incoming, reflected and transmitted light, using a Maxwell-Bloch simulator.	37
3.11	Absorption spectrum using the Maxwell-Bloch (MB) model, including the computed profiles and the original for comparison.	38
4.1	Supergaussian shaped, frequency-chirped readout pulse.	52
4.2	The simulated electric fields, being the incoming, reflected and the transmitted, in case 3.	53
4.3	Transmission and reflection spectra. Case 1, with medium cavity detuning.	55

4.4	Calculated absorpition spectrum and error plot. Case 1.	55
4.5	Transmission and reflection spectra. Case 2, with a small cavity detuning.	56
4.6	Calculated absorpition spectrum and error plot. case 2.	56
4.7	An extra transmission and reflection spectrum with increased grid size in detuning. Case 2b.	57
4.8	Calculated absorpition spectrum and error plot. Case 2b.	57
4.9	Transmission and reflection spectra. Case 3, with no cavity detuning.	58
4.10	Calculated absorpition spectrum and error plot. Case 3.	58
4.11	Transmission and reflection spectra. Case 4, with a large cavity detuning.	59
4.12	Calculated absorpition spectrum and error plot. Case 4.	59
4.13	Absorption spectrum with different Signal to Noise Ratio (SNR), using method 1 on case 3.	60
4.14	Relative error between the original and computed absorption spectrum, for different SNR, when method 1 is used on case 3.	60
4.15	Absorption spectrum with different SNR, using method 2 on case 3.	61
4.16	Relative error between the original and computed absorption spectrum, for different SNR, when method 2 is used on case 3.	61
4.17	Absorption spectrum with different SNR, using method 2 on case 1.	62
4.18	Relative error between the original and computed absorption spectrum, for different SNR, when method 2 is used on case 1.	62
5.1	Hypothetical experimental setup.	65

Chapter 1

Introduction

This chapter is intended to serve as springboard for the rest of this thesis, so that the reader may have some fundamental understanding of the problem which this thesis treats. We begin with a small section covering the background of the quantum information field and then a short description of the optical quantum memory, which is the focus of this report.

After that we follow up with the problem description, the goal of the thesis and the suggested method. The chapter is concluded by describing the structure of the thesis.

1.1 Background

Quantum information [5] is a quickly developing field which covers the study of information processing which makes use of quantum mechanical systems. As such it is not only connected to research fields such as quantum mechanics and computer science, but also to fields like atomic physics and photonics when looking at hardware implementations. Examples of applications are quantum computers [5] and quantum cryptography [17].

The key concept in quantum information is the qubit, which is an analogous concept to that of bits in classical computing. They are similar in the sense that they can both have a state, which in the case of bit is 0 or 1. The qubit also chooses from two states, usually referred to as $|0\rangle$ and $|1\rangle$ using ket notation. The difference however is that the qubit can also form states which are a superposition or a combinations of several states, such as

$$|\psi\rangle = \alpha |0\rangle + \beta |1\rangle.$$

α and β are complex numbers which determines the overall state of the qubit. As such the qubit has a continuum of states to exist in, while the bit only has two definite states to choose from. This opens up a wide arrange of applications, such as those mentioned above.

The question is how to actually implement the qubit in reality. The answer is that it depends highly on the requirements of the particular application. The qubit particle of course has to obey quantum mechanics. For long range quantum communication, it's suitable to use photons, using for example its two polarization states to represent the qubit states. For long term local storage we

may instead choose to use electrons bound to molecules, and use the different energy levels as states.

Unfortunately, physical implementations are problematic since quantum states often in reality are extremely sensitive to any outside perturbations. One of the postulates in quantum mechanics is that any measurement will collapse the state, and ultimately destroy its original state. To overcome this problem one can of course try to reduce any outside perturbation and losses in the included components. However it's also possible to apply some quantum error correction methods [13], so there is some tolerance in this matter.

This report is related to the development of so called Optical Quantum Memories (OQMs) [3], whose purpose is to store incoming photons for some time duration, with the possibility to extract the photon once again with its quantum state intact.

One application is for example in the use of quantum repeaters [10], which serves as in between stations in long distance quantum communication. The purpose is to reduce effects such as absorption in the optical fibers used for transportation, since the chance of the photon being absorbed increases exponentially with the propagation length. Whatever the application is, there is always a demand of high efficiency of the memory.

The development of optical quantum memories is a wide field, with several possible solutions and experimental realisations presented. Variations include what type of material and scheme is used. Usually the main aspect is that the storage is conducted by some absorbing media, with some certain absorption profile. Some methods make use of controlled external electric fields, which allows the operator to control how the qubit is stored and extracted.

In the atomic physics department in Lund university, one particular scheme is under investigation. The method make use of so called Atomic Frequency Combs (AFCs), proposed in [16].

Theoretically this has been shown to provide an efficiency of 54%, in the forward direction, which may in some cases be sufficient but not optimal. Experimentally 35% has been shown in [1]. By efficiency we refer to how much of the information stored is recovered after extraction.

In [2] a modification of the AFC-scheme, which make use of cavities was suggested, which was theoretically proven to have near unit efficiency. A recent experimental result from Lund [14] using this technique resulted in an efficiency of 56%, which definitely raises the hope for a future highly efficient OQM.

1.2 Optical Quantum Memory

This section is by no means intended as a rigorous review of how an Optical Quantum Memory (OQM) works, the purpose is to give the reader some sense of the physics at work in the system. We will limit ourself to the case of OQMs which make use of the AFC-scheme.

The fundamental component of OQMs [3] is the absorbing medium, which is used to store an incoming qubit photon. This is only possible if the medium or system has a long coherence time¹ compared to the time in which the qubit is supposed to be stored. This is not the case in most quantum systems, where

¹The coherence time can be considered the time in which the phase development of the system is still predictable. It can also be thought of as the memory of the system.

interaction with surrounding atoms and perturbations from the outside destroys the stored qubit information far too rapidly.

The system [18] which is discussed in this thesis makes use of a crystal medium which has been doped with rare-earth ions and cooled down using liquid helium to temperatures around a few Kelvin. This results in some comparably long coherence times when looking at the optical excited states of the rare-earth ions. In [14] for example, the used rare-earth was praseodymium (a doping percentage of 0.05%), where the orbital transitions are used for the storage.

1.2.1 3-level system

We will not delve into any complicated energy level diagrams which is out of the scope of this thesis, and only assume that we have a set of energy levels to choose from, as is shown in figure 1.1 in which three levels are displayed, denoted the ground state $|g\rangle$, the excited state $|e\rangle$ and the auxiliary state $|aux\rangle$.

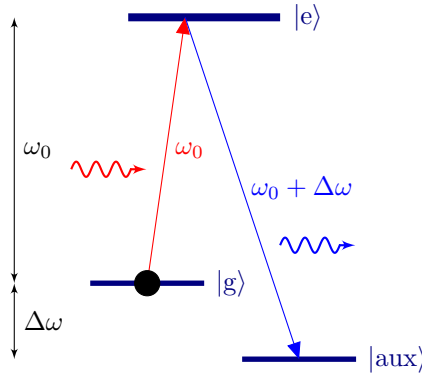


Figure 1.1: A 3-level energy diagram, including a ground state $|g\rangle$, an excited state $|e\rangle$ and an auxiliary state $|aux\rangle$, with an electron in the ground state. The transition energies are ω_0 between ground and excited state, and $\omega_0 + \Delta\omega$ between auxiliary and excited state. Note that ω_0 are many magnitudes larger than $\Delta\omega$, which is not displayed in the figure (ω_0 is in the order of THz while $\Delta\omega$ is likely in the order of MHz). The red and blue sinus-shaped arrows represent an incoming and emitted photon respectively.

The light-matter interaction can occur in three ways. An electron in the ground state can be moved up to the excited state $|e\rangle$ by absorption of an incoming photon with an optical frequency matching the transition frequency ω_0 . Transition from the excited down to either ground or auxiliary state occurs through either spontaneous emission or stimulated emission² [19], which either way produces an emitted photon of frequency corresponding to the transition.

An important feature of the transitions, is that due to the limited life time T (the time it takes for a spontaneous emission to occur) of the excited state, we get an homogeneous broadening³ in the transition spectrum [19], with a linewidth

²Stimulated emission is induced by another incoming photon of frequency corresponding to the transition.

³The transition lineshape function takes the form of a Lorentzian when looking at the transition spectrum.

of

$$\Gamma_h = \frac{1}{\pi T}. \quad (1.1)$$

In the case of a long life time, which is related to long coherence time (a desired feature), we receive a narrow linewidth.

1.2.2 Inhomogenous broadening

Now imagine our crystal with its ions which we assume operates in a three level system as in figure 1.1. If all ions share the same transition frequency, we have a light-matter interaction limited to a very narrow bandwidth of Γ_h , which may be as narrow as in the order of a few Hz [26]. This is suboptimal since we would rather have our OQM to be able to store photons of a wide range of frequencies.

However in reality there will be some sort of inhomogenous broadening over the lineshapes of the ions, due to imperfections in the crystal structure and the random distribution of the ions. This produces randomized variations in the surrounding of each ion, with the result that each separate ion receive a random alteration in its transition frequency. This feature is displayed in figure 1.2. We now have an ensemble of ions with a wide range of frequencies, which in the transition spectrum sums up as a broadened lineshape as seen in figure 1.2. The linewidth the inhomogenous broadening Γ_{inh} is typically in the GHz range [18].

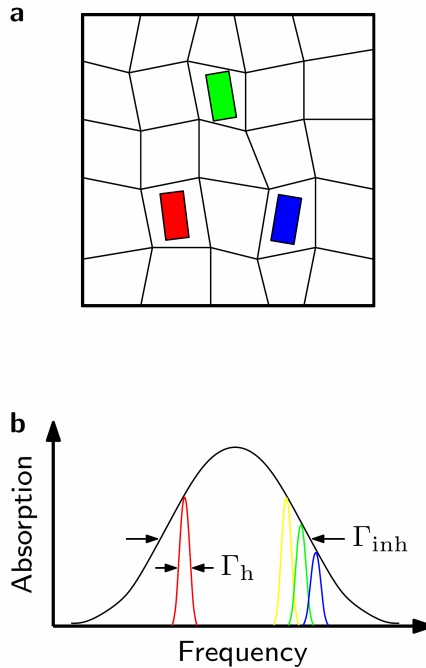


Figure 1.2: a) Due to the variations in the surroundings, each ion has an unique transition frequency (hence different colors). b) In the transition spectrum we thus get an inhomogeneous broadening with width Γ_{inh} , since the transition frequency is shifted in random fashion for each ion. The homogeneous linewidth Γ_h is very narrow in comparison to Γ_{inh} . Figure is taken from [18].

1.2.3 Absorption profile shaping

The nature of the inhomogeneous broadening is that if we excite ions on a certain frequency, the rest of the ions remain unaffected. This allows us to actively shape the structure in the absorption spectrum.

To follow the procedure, look again in figure 1.1 for reference. Burning a hole in the spectrum at frequency ω_0 is done by first exciting all ions in the ground state by using an intense light pulse of frequency ω_0 . The ions are then moved to the auxiliary state through spontaneous decay. Most of the ions with frequency ω_0 should now be in the auxiliary state $|\text{aux}\rangle$, and since this state has a long life time, they can in practice be considered to removed from the spectral shape. When looking at the transmission spectrum, this appears as a spectral hole at ω_0 , since there are no available ions with that frequency to absorb the light.

It's of course possible to refill the hole by exciting the ions from $|\text{aux}\rangle$ back to $|e\rangle$ through absorption of an incoming pulse with frequency $\omega_0 + \Delta\omega$. Since the homogeneous linewidth is so thin, it's possible to create very fine structures in transition profile.

1.2.4 AFC

In the Atomic Frequency Comb (AFC) scheme, the absorption profile is created by first burning a well structure over a range of a couple of MHz. Afterwards some ions in the well are brought back in such a way that we get periodic structure of peaks. An idealized absorption spectrum is shown in figure 1.3.

This structure allows an incoming light pulse to be stored in the ion ensemble which make up the AFC structure. Some requirements for good efficiency is that the spectral width of the pulse is not smaller than the distance between the peaks, but not larger than the full width of the AFC structure [21]. Other parameters which affect efficiency is the height of the peaks and side walls, and the finesse⁴ of the peaks, more can be read about this in [16].

So how is the photon qubit extracted from the crystal? After the absorption, the excited ions in the AFC peaks begin to oscillate with their respective transition frequency. Precisely at the beginning of the storage, all ions will be in phase, however since they all oscillate with different frequencies, they will immediately become out of phase with each other.

After a certain time the ions will return to be in phase again. This happens when the frequency ω_i for each AFC peak i is matched with each other, such that

$$T(\omega_{i+1} - \omega_i) = T\Delta\omega = 2\pi q,$$

where T is the storage time, q is some positive integer and $\Delta\omega$ the distance between the peaks.

The re-phasing then result in a remitted light pulse, with its original phase and qubit information preserved. Hence we don't have any direct control over the extraction time, which depends on the distance $\Delta\omega$ between the peaks.

A problem when using this method however is that the maximal efficiency is limited due to how a light pulse develops when propagating in the absorbing media. If the case is that of a short or weakly absorbing crystal, the pulse may

⁴The finesse is defined as the peak distance divided by the peak width.

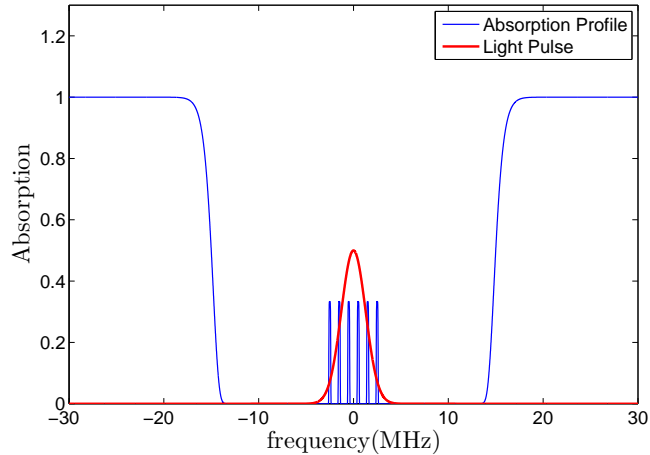


Figure 1.3: Absorption spectrum, utilizing the AFC scheme. The structure consist of a well structure with the AFC structure in the bottom, with an equidistant distance between the peaks. The width of the AFC structure is required to cover the spectral width of any pulse that is to be stored.

not be absorbed and just go right through the crystal. If the crystal is too long or the absorption is too high however, too much of any remitted light may be reabsorbed in the sample, before it has been able to leave the crystal. There is of course an optimal crystal length which maximizes the efficiency ⁵, however this is still a major limit.

1.2.5 Introducing a cavity

A method which solves the problem above is to use an optical cavities. In [2] it was shown that near unity efficiency can be achieved, by placing the absorbing crystal inside a cavity consisting of a semitransparent incoupling mirror and a highly reflective back mirror. Maximal efficiency is achieved when the impedance matching condition is fulfilled, which occurs when the absorption per round trip matches transmission of the mirrors. In [14] an experimental efficiency of 56% was achieved, which is major improvement relative to similar previous experiments, however we are still far from the near unity efficiency case.

An advantage is also that the required absorption strength of the medium is comparatively low (the low absorption is compensated by the multiple light round trips in the cavity), which makes the manufacturing process of the doped crystals easier.

In practice we construct the cavity by applying a reflective coating directly on the crystal, though one could use different setups such as placing the crystal in some sort of chamber.

⁵Maximum theoretical efficiency is 54 % [16].

1.3 Description of the problem

While higher efficiency has been shown in the case of using cavity, there is one fundamental problem using this method. As explained above, the efficiency of the storage is closely related to the shape of the absorption. In the case in which no cavity is present, it's quite straightforward to burn the absorption profile and measure the transmission through the crystal, in order to resolve the absorption spectrum. This is however not the case in a cavity crystal system.

The reflection and transmission from a cavity depends on both the mirror transmission and reflection coefficients, and the properties of the media inside. Due to the field build-up inside the cavity and the dispersive⁶ effects of absorbing media, the relation between the absorption inside the crystal, the input and output fields from the cavity is non-trivial. Hence we have no good way of looking at what's happening inside the media.

The same argument can be applied when we burn the absorption profile. It may very well be that the resulting structure does not correspond to the desired one, and we have no easy way of even determining if this is the case. Figure 1.4 illustrates this problem.

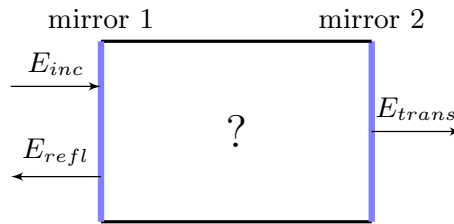


Figure 1.4: A conceptual illustration of the cavity with the absorption medium and the outside fields. The problem is that there is currently no simple way to conclude how the absorption spectrum look inside the cavity.

The reader may wonder why one just can't send the burning and measuring pulse orthogonally relative to the cavity length and thus bypass the mirrors and the cavity. There are several reasons for this, one being that it's easier to let the burning, measuring and storage pulses propagate along the same path, hence the convenience reason. However the fact is also that the burned structure is also very localized in space, which limits the path which different beams can take in order to interact with the modified absorption spectrum.

It's also not possible to for a short duration remove the mirrors from the crystal to burn and measure the spectrum, and then put them back for the actual storage, since the mirrors are actually composed of a coating which are not removed easily or quickly.

To summarize the problem, due to the fact that we have a non-linear interaction between the cavity structure and the crystal absorption spectrum, the procedure of burning and mapping the absorption spectrum in the crystal becomes non-trivial. We simply can't say how the structure actually looks inside the cavity in an easy way.

⁶A medium with frequency varying absorption are dispersive, meaning that different frequency components travel at different refractive index or speed.

1.4 Aim of this thesis

This thesis is mainly aimed to provide a solution the problem above. There are several hypothetical ways of doing this. One could for example develop a way to simulate the burning process and then assume that doing the same thing in reality provides the same result.

Another method is to develop some sort of Analysing Tool (AT) which takes the output from a cavity crystal with unknown absorption spectrum, and reversely calculates the spectrum. If the spectrum differs from the desired spectrum, one can make adjustments to the burning process and repeat the process until satisfaction.

Ultimately both of these methods are important in order to gain complete control over the system and achieve a near perfect OQM efficiency. We both need to know how to actually burn the desired spectrum and to be able to control that the resulting spectrum is the desired one, since there in reality always are uncertainties.

This thesis will focus on the later method, i.e. the development of an AT.

1.5 Solution

The development of the solution is presented in two stages. First we need to understand the processes happening in the cavity, relating to the cavity structure and the interaction between the light and the medium. An analysing tool which fulfils the requirements can then be developed.

In order to assert the correctness of the method, it's suggested that the process in the cavity is simulated using a known set of parameters. The assessment of the analysing method is conducted as follows.

1. Run a simulation of the system, knowing all parameters including the absorption profile, which results in some kind of output.
2. Apply the analysing tool on the output from the simulation, which should result in a computed hypothetical absorption spectrum.

An attempt at visualizing the process can be seen in figure 1.5. If the computed spectrum equals the original, we can assume that the tool in this case result in a correct mapping of the absorption spectrum.

It should be noted that there is also the question concerning how sensitive the method will be to errors in the measurements, as well as how complicated the tool actually is to implement in reality. In the numerical or theoretical case it's easier to have control over the relative processes and parameters, however this is not true in the experimental or real case, in which the actual application of the subject lies.

1.6 Structure

We conclude the introduction chapter by commenting on the structure of the thesis. The parts included are as follows.

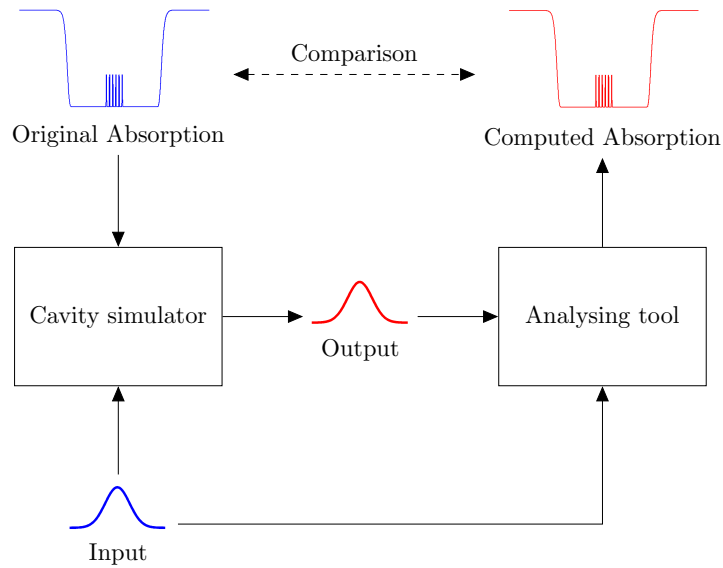


Figure 1.5: An illustration on how to determine the performance of the analysing tool. It begins with the simulation of the system at hand, using some input field and a predefined absorption profile. The resulting output is then, along with the input fields, processed in the analysing tool, with some absorption profile as a result. The task is then to compare the computed absorption profile with the original.

- The *Theory* chapter, which is aimed at presenting some fundamental theory required for understanding the subject at hand. Some specific derivations are left out for later when they are more relevant.
- The *Analysing tool* chapter, in which the derivation of the algorithm is presented, which will be used to compute the absorption spectrum. It will be concluded with a result section, in which we assess its performance on simulated data, using third-person developed code.
- The *Maxwell-Bloch simulator* chapter, we try to complement with some simulations of our own, due to reasons stated in the previous chapter.
- The *Experiment* chapter, which broadly discusses the experimental stage of the project.

Chapter 2

Theory

This part is aimed at providing the knowledge and formalism needed in order to understand and treat the problem at hand.

The process inside the material is described by representing the light in the classical picture, while the matter interaction with light is described quantum mechanically, using a two level system.

One should mention that while representing a field in a complex valued way may be of a mathematical convenience, complex valued fields in quantum mechanics have an actual physical interpretation. Therefore one has to take care when interchanging the two models.

2.1 Electric field representation

In this thesis we assume that the field has its origin from a laser source, which has a certain central radial frequency ω_L , chosen so that it's close to the transition frequencies in the absorbing medium, and is frequency modulated in some way. Note that we usually refer to the radial frequency in derivations which is usually denoted ω with units [rads^{-1}], while we prefer to use the ordinary frequency $\nu = \omega/(2\pi)$ with units [Hz] for plots. When commenting on values of frequency, we always use [Hz].

The main idea throughout this chapter is that we want to extract all exponential terms containing ω_L . This simplifies our equations and more importantly reduces the workload in a numerical setup. ω_L can be considered to be very high, in the order THz, and the bandwidth of our absorption spectra will be in the MHz range, so it's more sensible too look at the the frequency difference from ω_L , which we refer to as the detuning, denoted by δ .

The coordinate system is chosen so that the field is pointing along the x-axis, while propagating along the z-axis, as

$$\mathbf{E}(z, t) = E(z, t)\hat{\mathbf{e}}_x. \quad (2.1)$$

We have here assumed that the light is linearly polarized. In our cavity system, the field is composed of an forward and backward propagating field $E_+(x, t)$

and $E_-(x, t)$ respectively, as

$$\begin{aligned} E(z, t) &= E_+(x, t) + E_-(x, t) \\ &= \xi_+(z, t) \cos(\omega_L t - k_L z + \varphi_+(t)) + \xi_-(z, t) \cos(\omega_L t + k_L z + \varphi_-(t)), \end{aligned} \quad (2.2)$$

where ξ_+ and ξ_- are the real-valued envelopes of the forward and backward propagating components respectively, and $\varphi_+(t)$ and $\varphi_-(t)$ are some time-dependant phase functions. Also note that $k_L = \omega_L/c$, is the central wavenumber of the laser.

The wave can be rewritten to

$$\begin{aligned} E(z, t) &= \frac{\mathcal{E}_+}{2} e^{i(\omega_L t - k_L z)} + \frac{\mathcal{E}_+^*}{2} e^{-i(\omega_L t - k_L z)} + \dots \\ &\quad + \frac{\mathcal{E}_-}{2} e^{i(\omega_L t + k_L z)} + \frac{\mathcal{E}_-^*}{2} e^{-i(\omega_L t + k_L z)}, \end{aligned} \quad (2.3)$$

where \mathcal{E}_+ and \mathcal{E}_- are given by

$$\mathcal{E}_+ = \xi_+(z, t) e^{i\varphi_+(t)} \quad (2.4)$$

$$\mathcal{E}_- = \xi_-(z, t) e^{i\varphi_-(t)}. \quad (2.5)$$

A convenient way of representing the field is using vectors with separate elements for forward and backward fields, such as

$$\mathbf{E} = \mathbf{E}(z, t) = \begin{pmatrix} \mathcal{E}_+(z, t) \\ \mathcal{E}_-(z, t) \end{pmatrix}. \quad (2.6)$$

The original field can be attained by

$$\begin{aligned} E(z, t) &= \frac{1}{2} \left\{ \mathbf{e}^T \mathbf{E} e^{i\omega_L t} + (\mathbf{e}^T \mathbf{E})^* e^{-i\omega_L t} \right\}, \\ &= \frac{1}{2} \left\{ \mathbf{e}^T \mathbf{E} e^{i\omega_L t} + \mathbf{e}^\dagger \mathbf{E}^* e^{-i\omega_L t} \right\}, \\ &= \frac{1}{2} \left\{ \mathbf{e}^T \mathbf{E} e^{i\omega_L t} + c.c. \right\}, \end{aligned} \quad (2.7)$$

where

$$\mathbf{e} = \mathbf{e}(z, t) = \begin{pmatrix} e^{-ik_L z} \\ e^{ik_L z} \end{pmatrix}. \quad (2.8)$$

We use the term *c.c.* to denote the complex conjugate part of the field. Note that \mathbf{T} indicates transpose, star ($*$) complex conjugate and dagger (\dagger) complex transpose. Some useful formulas for later use are

$$\mathbf{e}^T \mathbf{E} = \mathbf{E}^T \mathbf{e}, \quad (2.9)$$

and

$$\mathbf{e}^\dagger \mathbf{e} = 2. \quad (2.10)$$

Representing the field as in 2.7, using the laser frequency $\omega_L t$ and \mathbf{e} as a reference frame, is the first step in simplifying the equations later on.

2.2 Maxwell equations

The Maxwell equations [19] are

$$\nabla \times \mathbf{E} = -\frac{\partial \mathbf{B}}{\partial t}, \quad (2.11)$$

$$\nabla \times \mathbf{H} = \mathbf{J} + \frac{\partial \mathbf{D}}{\partial t}, \quad (2.12)$$

$$\nabla \cdot \mathbf{D} = \rho, \quad (2.13)$$

$$\nabla \cdot \mathbf{B} = 0, \quad (2.14)$$

$$(2.15)$$

where \mathbf{D} is the electrical displacement field, \mathbf{B} the magnetic flux, \mathbf{H} the magnetic field, \mathbf{J} the electrical current and ρ is the total free charge. It's assumed that there are no free charges present, hence $\rho = 0$ and $\mathbf{J} = 0$. It's also assumed that there is no magnetization in the material.

The material can then be assumed to be modelled by the following equations

$$\mathbf{D} = n^2 \epsilon_0 \mathbf{E} + \mathbf{P}, \quad (2.16)$$

$$\mathbf{B} = \mu_0 \mathbf{H}, \quad (2.17)$$

where μ_0 is the permeability constant, n the refractive index of the host material, ϵ_0 is the permittivity constant and \mathbf{P} the polarization induced by the doped ions.

Some explanation of the equations above may be in order. The upper equation states that the electrical displacement field, which takes into account the displacement of free and bound charges in the material, is composed of two parts. The first term $n^2 \epsilon_0 \mathbf{E}$ takes the the host material into account, assuming that there is no absorption or scattering present. The second term is a general polarization term, which takes into account the induced dipole moments of the doped ions in the material. The lower equation states that since we have no magnetization in the material, we can set the magnetic flux to proportional the magnetic field.

Before we can set up a practical equation system, we note that we can assume that cavity contains no transversal modes and propagates along the z -axis (along the cavity) with the field components directed along the x -axis. See figure 2.1 for an illustration.

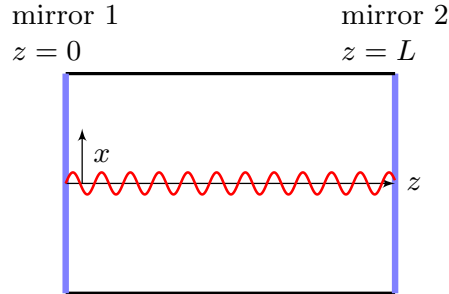


Figure 2.1: An illustration of the electric field propagation inside the cavity crystal, with field component along the x -axis and propagation along the z -axis.

Inserting the equations above into the Maxwell equations yields after some algebra,

$$\frac{\partial^2 E}{\partial z^2} - \frac{n^2}{c_0^2} \frac{\partial^2 E}{\partial t^2} = \mu_0 \frac{\partial^2 P}{\partial t^2}, \quad (2.18)$$

with $c_0 = 1/\sqrt{\mu_0\epsilon_0}$ is speed of light in vacuum. The polarization is defined as the average dipole moment per volume unit, being

$$P(z, t) = \frac{N}{2\pi V} \int_{-\infty}^{\infty} g(\delta) p_x(z, t, \delta) d\delta, \quad (2.19)$$

with $g(\delta)$ being the distribution of ions with detuning δ , V the volume, $p_x(z, t, \delta)$ the dipole moment of an single ions and N the number of ions. We make the assumption that the ions are homogeneously spread out in the sample. Condition for g is

$$\int_{-\infty}^{\infty} g(\delta) d\delta = 2\pi. \quad (2.20)$$

This term has its origin in [15].

The problem is now to determine the expression for the dipole moment p_x for the ions, which represents the light-matter interaction in 2.18. This will be done quantum mechanically in the next section.

2.3 Bloch equations

This section covers the Bloch equations, which serve to model the interaction between light and matter in our system. The derivations presented here have are covered in similar fashion in [8], however for a more stringent covering one can use [15].

In figure 1.1 a 3-level system was discussed, however we will limit ourself by only considering a 2-level system. This is reasonable since any ions in $|\text{aux}\rangle$ can be considered to be non-interacting in the frequency regime we are looking at. The system is then described by the states $|\psi_g\rangle$ and $|\psi_e\rangle$ representing the ground and excited state respectively. The transition radial frequency is ω_0 . Also we assume that the two states form an orthonormal space.

The Bloch sphere, shown in figure 2.2 with states $|0\rangle$ and $|1\rangle$, is a recurring concept in quantum mechanics, since it in a intuitive way depicts the state in which a two level system can exist in, where the south and north poles represent the states where we have either full population in either the ground or excited state. All other points are states which are superpositions between these.

The state of the system is defined by the Bloch vector which points to a certain coordinate at the sphere.

2.3.1 Hamiltonian

The system is described by the Hamiltonian

$$H(z, t) = H_0 + H_p(z, t). \quad (2.21)$$

H_0 is the Hamiltonian for the unperturbed system, with eigenvalues $\omega_g\hbar$ and $\omega_e\hbar$, for state $|\psi_g\rangle$ and $|\psi_e\rangle$ respectively, and H_p is the perturbation from

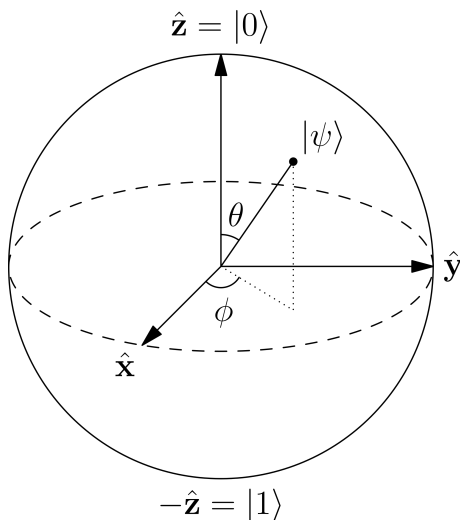


Figure 2.2: The Bloch sphere with states $|0\rangle$ and $|1\rangle$, which surface represents the states in which a 2-level system can exist in. Figure is taken from [24].

an external electric field $\mathbf{E}(\mathbf{z}, t)$, which we describe by

$$H_p(z, t) = e\mathbf{r} \cdot \mathbf{E}(\mathbf{z}, t) = exE(z, t), \quad (2.22)$$

The scalar product disappear since the field is assumed to be parallel to the x-axis. The detuning with respect to ω_0 is defined as

$$\delta = \omega_0 - \omega_L. \quad (2.23)$$

The system will be treated as a single ion system, though we in our case have an ensemble of multiple ions (Single ion storage is also possible). This is only a problem if there is significant interaction between the separate systems, which we claim to not be the case in our medium, which has fairly low doping levels (hence long distance between individual ions).

2.3.2 Rabi frequency

We will in this section make no assumptions of whether the wave consist of a forward and backward component, and only assume that the field is in the form

$$\begin{aligned} E(z, t) &= \xi(z, t)e^{i\varphi(t)}e^{i\omega_L t} + \xi(z, t)^*e^{-i\varphi(t)}e^{-i\omega_L t} \\ &= \xi(z, t)e^{i\varphi(t)}e^{i\omega_L t} + c.c. \end{aligned} \quad (2.24)$$

The Rabi frequency of the field is given by

$$\Omega = \frac{\mu_{ge}\xi(z, t)e^{i\varphi(t)}}{\hbar}, \quad (2.25)$$

where μ_{ge} is the transition dipole moment between ground and excited state along the x-coordinate, given by

$$\mu_{ge} = -e \langle \psi_g | x | \psi_e \rangle = -e \int \psi_g^* x \psi_e d^3\mathbf{r}. \quad (2.26)$$

Note that $\mu_{ge} = \mu_{eg}$ ¹ and it's important that $\xi(z, t)e^{i\varphi(t)}$ is assumed to vary slowly in the z-direction, in the sense that it can be considered constant in the domain of a single ion.

The electric field can now be written as

$$E(z, t) = \frac{\hbar}{2\mu_{ge}} \{ \Omega e^{i\omega_L t} + \Omega^* e^{-i\omega_L t} \}, \quad (2.27)$$

The Rabi frequency is a measure of the strength of the slowly varying field component, and is useful since it will simplify the equations later on.

2.3.3 Schrödinger equation

Inserting the field into the Schrödinger equation [8]

$$i\hbar \frac{\partial |\psi\rangle}{\partial t} = H |\psi\rangle, \quad (2.28)$$

and by assuming a solution in the form

$$|\psi\rangle = c_g e^{-i\omega_g t} |\psi_g\rangle + c_e e^{-i(\omega_g + \omega_0)t} |\psi_e\rangle, \quad (2.29)$$

we end up with equation

$$\begin{aligned} i\hbar [\dot{c}_g - i\omega_g c_g] e^{-i\omega_g t} |\psi_g\rangle + i\hbar [\dot{c}_e - i(\omega_g + \omega_0)c_e] e^{-i(\omega_g + \omega_0)t} |\psi_e\rangle = \\ = \hbar\omega_g c_g e^{-i\omega_g t} |\psi_g\rangle + \hbar(\omega_g + \omega_0)c_e e^{-i(\omega_g + \omega_0)t} |\psi_e\rangle + H_p(z, t) |\psi\rangle \end{aligned}$$

\Leftrightarrow

$$i\hbar \dot{c}_g e^{-i\omega_g t} |\psi_g\rangle + i\hbar \dot{c}_e e^{-i(\omega_g + \omega_0)t} |\psi_e\rangle = H_p(z, t) |\psi\rangle$$

Since $\langle \psi_g | \psi_e \rangle = \langle \psi_e | \psi_g \rangle = 0$ and $\langle \psi_g | \psi_g \rangle = \langle \psi_e | \psi_e \rangle = 1$ due to the orthonormality of the system, we can separate the equation into a equation system by multiplying with $\langle \psi_g |$ and $\langle \psi_e |$ from the left side separately, resulting in equation system

$$\begin{aligned} i\hbar \dot{c}_g e^{-i\omega_g t} &= \langle \psi_g | H_p(z, t) | \psi \rangle, \\ i\hbar \dot{c}_e e^{-i(\omega_g + \omega_0)t} &= \langle \psi_e | H_p(z, t) | \psi \rangle. \end{aligned} \quad (2.30)$$

To evaluate the right hand side terms, we need to make some assumptions and one approximation. The upper right term expands into

$$\langle \psi_g | H_p(z, t) | \psi \rangle = \left[e \langle \psi_g | x E(z, t) | \psi_g \rangle c_g e^{-i\omega_g t} + e \langle \psi_g | x E(z, t) | \psi_e \rangle c_e e^{-i(\omega_g + \omega_0)t} \right].$$

By assuming that the field vary slowly in space in the vicinity of the particle, we can approximate the field as constant, meaning that we can extract it from the braket products,

$$\langle \psi_g | H_p(z, t) | \psi \rangle = E(z, t) \left[e \langle \psi_g | x | \psi_g \rangle c_g e^{-i\omega_g t} - \mu_{ge} c_e e^{-i(\omega_g + \omega_0)t} \right].$$

¹We assume that the states are symmetrical with the respect to the spatial coordinates.

Here we've also used 2.26 to insert μ_{ge} . The first term in right side equals zero due to the symmetry properties mentioned above. Removing this term and inserting the expression for the field in 2.27, result in

$$\begin{aligned}\langle \psi_g | H_p(z, t) | \psi \rangle &= -\frac{\hbar}{2\mu_{ge}} \{ \Omega e^{i\omega_L t} + \Omega^* e^{-i\omega_L t} \} \mu_{ge} c_e e^{-i(\omega_g + \omega_0)t} \\ &= -\frac{\hbar c_e}{2} e^{-i\omega_g t} \{ \Omega e^{i(\omega_L - \omega_0)t} + \Omega^* e^{-i(\omega_L + \omega_0)t} \}\end{aligned}$$

The first term contains an exponent with the detuning frequency $\delta = \omega_0 - \omega_L$, however the other term contains frequency $\omega_L + \omega_0$. Since the laser frequency and transition frequency is assumed to be close to each other, we have one term oscillating relatively slowly, and one oscillating very rapidly. It's then reasonable to assume that this term will average out itself to zero over reasonable time steps, hence we can neglect this term. This approximation is usually referred to as the *Rotating wave approximation* [4, 9, 22]. Thus we receive

$$\langle \psi_g | H_p(z, t) | \psi \rangle = -\frac{\hbar c_e}{2} e^{-i\omega_g t} \Omega e^{-i\delta t}. \quad (2.31)$$

The exact same procedure result in

$$\langle \psi_e | H_p(z, t) | \psi \rangle = -\frac{\hbar c_g}{2} e^{-i\omega_g t} \Omega^* e^{-i\omega_L t}. \quad (2.32)$$

Inserting into our equation system in 2.30 result in

$$\begin{aligned}i\hbar \dot{c}_g e^{-i\omega_g t} &= -\frac{\hbar c_e}{2} e^{-i\omega_g t} \Omega e^{-i\delta t}, \\ i\hbar \dot{c}_e e^{-i(\omega_g + \omega_0)t} &= -\frac{\hbar c_g}{2} e^{-i\omega_g t} \Omega^* e^{-i\omega_L t}.\end{aligned} \quad (2.33)$$

Some further rearrangement finally result in

$$\begin{aligned}\dot{c}_g &= i\frac{\Omega}{2} e^{-i\delta t} c_e, \\ \dot{c}_e &= i\frac{\Omega^*}{2} e^{i\delta t} c_g.\end{aligned} \quad (2.34)$$

Hence we have a model for the evolution of the quantum state $|\psi\rangle$ in time.

2.3.4 Dipole moment

The output we are interested in is the resulting dipole moment, which is given along the x-axis by

$$\begin{aligned}p_x(t) &= -e \langle \psi | x | \psi \rangle = -e \int \psi^* x \psi d^3\mathbf{r} = \\ &= \mu_{ge} [c_g c_e^* e^{i\omega_0 t} + c_g^* c_e e^{-i\omega_0 t}] = \mu_{ge} [\rho_{ge} e^{i\omega_0 t} + \rho_{eg} e^{-i\omega_0 t}]\end{aligned} \quad (2.35)$$

The terms ρ are the elements of the density matrix

$$\boldsymbol{\rho} = |\psi\rangle \langle \psi| = \begin{pmatrix} \rho_{gg}(z, t) & \rho_{ge}(z, t) \\ \rho_{eg}(z, t) & \rho_{ee}(z, t) \end{pmatrix} = \begin{pmatrix} c_g c_g^* & c_g c_e^* \\ c_g^* c_e & c_e c_e^* \end{pmatrix}. \quad (2.36)$$

This is an useful formalism for treating a two level system, however in this report we will only make use of the elements. The terms ρ_{gg} and ρ_{ee} represent the expectation value of finding the electron in the ground and excited stated respectively. If we are looking at a macroscopic system of N systems, then $N\rho_{ee}$ for example is the average population in the excited state.

Further we have that ρ_{ge} and ρ_{eg} are the coherence between the states. As seen 2.35, it's the coherence terms which drives the dipole at the transition frequency.

We want to express the dipole in the form

$$p_x(z, t, \delta) = \frac{\mu_{ge}}{2} \{ (u + iv)e^{i\omega_L t} + (u - iv)e^{-i\omega_L t} \}, \quad (2.37)$$

since this is similar to the electric field in 2.27 or 2.7. u and v are given by

$$\begin{aligned} u &= \{ e^{i\delta t} \rho_{ge} + e^{-i\delta t} \rho_{eg} \}, \\ v &= -i \{ e^{i\delta t} \rho_{ge} - e^{-i\delta t} \rho_{eg} \}. \end{aligned} \quad (2.38)$$

2.3.5 Complete Bloch equation

Now to find a solution to u and v . Using 2.34, we get

$$\dot{\rho}_{ge} = \frac{\partial(c_g c_e^*)}{\partial t} = \dot{c}_g c_e^* + c_g \dot{c}_e^* = i \frac{\Omega}{2} e^{-i\delta t} c_e c_e^* + c_g \left(-i \frac{\Omega}{2} e^{-i\delta t} c_g^* \right), \quad (2.39)$$

$$\dot{\rho}_{eg} = \frac{\partial(c_g c_e^*)}{\partial t} = \dot{c}_g c_e^* + c_g \dot{c}_e^* = -i \frac{\Omega^*}{2} e^{i\delta t} c_e^* c_e + c_g^* \left(i \frac{\Omega}{2} e^{i\delta t} c_g \right), \quad (2.40)$$

$$\dot{\rho}_{ee} = \frac{\partial(c_e c_e^*)}{\partial t} = \dot{c}_e c_e^* + c_e \dot{c}_e^* = i \frac{\Omega^*}{2} e^{i\delta t} c_g c_e^* + c_e \left(-i \frac{\Omega}{2} e^{-i\delta t} c_g^* \right). \quad (2.41)$$

Using the elements in the density matrix, above simplifies into

$$\dot{\rho}_{ge} = i \frac{\Omega}{2} e^{-i\delta t} (\rho_{ee} - \rho_{gg}) - \frac{\Gamma}{2} \rho_{ge}, \quad (2.42)$$

$$\dot{\rho}_{eg} = -i \frac{\Omega^*}{2} e^{i\delta t} (\rho_{ee} - \rho_{gg}) - \frac{\Gamma}{2} \rho_{eg}, \quad (2.43)$$

$$\dot{\rho}_{ee} = i \frac{\Omega^*}{2} e^{i\delta t} \rho_{ge} - i \frac{\Omega}{2} e^{-i\delta t} \rho_{eg} - \Gamma \rho_{ee}. \quad (2.44)$$

The terms containing Γ are included above, so that decay from the excited state to the ground state is taken into account. This means that without a driving field Ω , ρ_{ee} will decay by a factor $e^{-\Gamma t}$ or $e^{-t/T}$, where T is the lifetime of the excited state, related to the decay as $T = 1/\Gamma$.

In matrix form the system translates to

$$\dot{\rho} = \mathbf{A}' \rho, \quad (2.45)$$

where

$$\boldsymbol{\rho} = \begin{pmatrix} \rho_{ge} \\ \rho_{eg} \\ \rho_{ee} \end{pmatrix}, \quad (2.46)$$

$$\mathbf{A}' = \begin{pmatrix} -\frac{\Gamma}{2} & 0 & -i\frac{\Omega}{2}e^{-i\delta t} \\ 0 & -\frac{\Gamma}{2} & i\frac{\Omega^*}{2}e^{i\delta t} \\ i\frac{\Omega^*}{2}e^{i\delta t} & -i\frac{\Omega}{2}e^{-i\delta t} & -\Gamma \end{pmatrix}. \quad (2.47)$$

We are now interested in transforming the system to include the u and v components. We note that $\rho_{gg} + \rho_{ee} = 1$ and introduce a third component $w = \rho_{gg} - \rho_{ee}$, which can be regarded as measurement of the population difference between the states. Then we have that

$$w = 1 - 2\rho_{ee}. \quad (2.48)$$

The Bloch vector \mathbf{R} , is described by

$$\mathbf{R} = \mathbf{R}(z, t) = \begin{pmatrix} u \\ v \\ w \end{pmatrix}. \quad (2.49)$$

Using 2.38 and 2.48, we get the relation

$$\mathbf{R} = \mathbf{T}\boldsymbol{\rho} + \boldsymbol{\varphi}', \quad (2.50)$$

where

$$\mathbf{T} = \begin{pmatrix} e^{i\delta t} & e^{-i\delta t} & 0 \\ -ie^{i\delta t} & ie^{-i\delta t} & 0 \\ 0 & 0 & -2 \end{pmatrix}, \quad (2.51)$$

$$\boldsymbol{\varphi}' = \begin{pmatrix} 0 \\ 0 \\ 1 \end{pmatrix} \quad (2.52)$$

The system can now be described by the Bloch vector, by using the transformation matrix \mathbf{T} . We get

$$\begin{aligned} \dot{\mathbf{R}} &= \frac{\partial(\mathbf{T}\boldsymbol{\rho} + \boldsymbol{\varphi}')}{\partial t} = \dot{\mathbf{T}}\boldsymbol{\rho} + \mathbf{T}\dot{\boldsymbol{\rho}} = \dot{\mathbf{T}}\mathbf{T}^{-1}(\mathbf{R} - \boldsymbol{\varphi}') + \mathbf{T}\mathbf{A}'\boldsymbol{\rho} = \\ &= \dot{\mathbf{T}}\mathbf{T}^{-1}\mathbf{R} + \mathbf{T}\mathbf{A}'\mathbf{T}^{-1}(\mathbf{R} - \boldsymbol{\varphi}') = \\ &= \mathbf{A}\mathbf{R} + \boldsymbol{\varphi}. \end{aligned} \quad (2.53)$$

Some algebra yields

$$\mathbf{A} = \begin{pmatrix} -\frac{\Gamma}{2} & -\delta & -\frac{i}{2}(\Omega - \Omega^*) \\ \delta & -\frac{\Gamma}{2} & -\frac{i}{2}(\Omega + \Omega^*) \\ \frac{i}{2}(\Omega - \Omega^*) & \frac{1}{2}(\Omega + \Omega^*) & -\Gamma \end{pmatrix}, \quad (2.54)$$

$$\boldsymbol{\varphi} = \begin{pmatrix} 0 \\ 0 \\ \Gamma \end{pmatrix}. \quad (2.55)$$

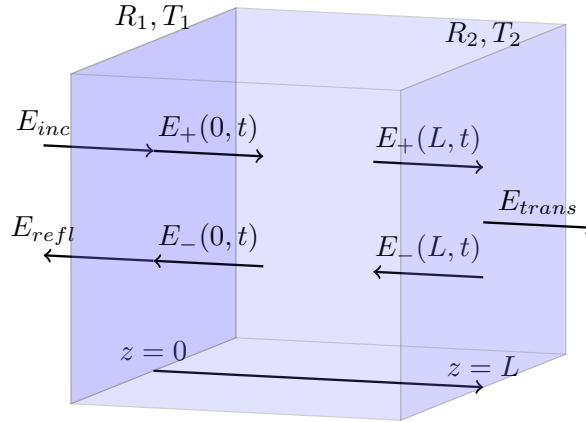


Figure 2.3: Cavity crystal with two semitransparent mirrors at each side, denoted mirror 1 and 2. At the left side we have an incoming and a reflected field travelling in the forward and backward direction respectively. At the right side we have a transmitted and an incoming field.

We now have the tools to fully model the time progression of the Bloch vector, where the components $u(\delta)$ and $v(\delta)$ are required for the dipole moment $p_x(\delta)$. We will come back to this equation in the the Maxwell-Bloch simulator chapter.

2.4 Cavity

The cavity is in essence composed of two semitransparent mirrors with some medium inside. This section will mostly be dedicated to discuss how the electric field outside will interact with the inside field, however some basic resonator optics theory is also in order since this will later on be useful in order to make sure that the simulator used actually can simulate basic phenomena.

2.4.1 Cavity mirrors

The cavity consist of two mirrors which we refer to as mirror 1 and 2, being the left and right mirror, which in reality are composed of some sort of dielectric coating. We also assume that the refractive index of the cavity host material is higher than the outside index, likely being air ($n = 1$). A principal picture of the cavity is shown in figure 2.3, with notations included. The length of the cavity is denoted as L .

Consider an semitransparent mirror interface with some reflection R and transmission², relating to each other as

$$R + T = 1. \quad (2.56)$$

Hence we have no absorption in the interface. We assume for simplicity that the

² R and T measure how much of the *intensity* T of the field is reflected and transmitted respectively.

mirrors are either infinitely thin or simply doesn't change the fields propagating through in any notable way.

At mirror 1, positioned at $z = 0$ we assume an incoming field E_{inc} at the left side, propagating in the forward direction, and a reflected field E_{refl} propagating in the backward direction at the left side. The field at the right side are denoted $E_+(0, t)$ and $E_-(0, t)$ for the forward and backward propagating field respectively. Look in figure 2.3 for an illustration.

$$E_+(0, t) = t_1 E_{inc} + r_1 E_-(0, t), \quad (2.57)$$

$$E_{refl} = -r_1 E_{inc} + t_1 E_-(0, t). \quad (2.58)$$

Here $t_1 = \sqrt{T_1}$ and $r_1 = \sqrt{T_1}$ are the reflection and transmission coefficients for mirror 1. Note that the minus sign in the lower equation is due to the fact that reflection at a surface with higher reflective index introduces a phase change of π . By representing the fields as in 2.6 and after some rearranging, we get

$$\mathbf{E}_1 = \mathbf{T}_1 \mathbf{E}_0, \quad (2.59)$$

where

$$\mathbf{T}_1 = \frac{1}{t_1} \begin{pmatrix} 1 & r_1 \\ r_1 & 1 \end{pmatrix} \quad (2.60)$$

and

$$\mathbf{E}_1 = \begin{pmatrix} E_+(0, t) \\ E_-(0, t) \end{pmatrix}, \quad (2.61)$$

$$\mathbf{E}_0 = \begin{pmatrix} E_{inc} \\ E_{refl} \end{pmatrix}. \quad (2.62)$$

Matrix \mathbf{T}_1 can as such be used to relate the incoming and outgoing fields outside the cavity to those directly inside.

For mirror 2, positioned at $z = L$ we have equation system

$$E_{trans} = t_2 E_-(L, t) - r_2 E'_{inc}, \quad (2.63)$$

$$E_-(L, t) = r_2 E_+(L, t) + t_2 E'_{inc}, \quad (2.64)$$

where E_{trans} is the transmitted field at the right side, propagating in the forward direction. Further E'_{inc} is the incoming field at the right side, while E_2^+ and E_2^- are forward and backward propagating field left of the mirror inside the cavity, illustrated in the figure as before. Note that E'_{inc} in our report will always be zero (we only have one incoming field from the left side), it's only included here for completeness.

Same procedure as above yields

$$\mathbf{E}_{trans} = \mathbf{T}_2 \mathbf{E}_2, \quad (2.65)$$

where

$$\mathbf{T}_2 = \frac{1}{t_2} \begin{pmatrix} 1 & -r_2 \\ -r_2 & 1 \end{pmatrix} \quad (2.66)$$

and

$$\mathbf{E}_2 = \begin{pmatrix} E_+(L, t) \\ E_-(L, t) \end{pmatrix}, \quad (2.67)$$

$$\mathbf{E}_{trans} = \begin{pmatrix} E_{trans} \\ E'_{inc} \end{pmatrix}. \quad (2.68)$$

This matrix is valid for the right mirror.

Note that we for the inverses of \mathbf{T}_1 and \mathbf{T}_2 have

$$\mathbf{T}_1^{-1} = \frac{1}{t_1} \begin{pmatrix} 1 & -r_1 \\ -r_1 & 1 \end{pmatrix}, \quad (2.69)$$

$$\mathbf{T}_2^{-1} = \frac{1}{t_2} \begin{pmatrix} 1 & r_2 \\ r_2 & 1 \end{pmatrix}. \quad (2.70)$$

2.4.2 Cavity modes

As mentioned above, it is of interest to present some fundamental theory on how cavities behave, in order to verify the simulator later presented. More can be read in [19].

Usually when discussing cavities, we talk about the cavity modes. We then refer to the certain frequencies where the interference between the forward and backward fields in the cavity interfere constructively, which in our case will result in a high transmission through the cavity. This happens when a full round trip in the cavity (which in propagation length corresponds to $2L$, two times the cavity length), matches some multiple of the wavelength of the field. In equation form this looks like

$$q\lambda_q = 2L, \quad q = 1, 2, 3, \dots \quad (2.71)$$

where λ_q is the cavity mode wavelength and q the cavity mode number. In frequency we have instead

$$\nu_q = \frac{c_0 q}{2nL}, \quad q = 1, 2, 3, \dots \quad (2.72)$$

where c_0 is the speed of light in vacuum and n the refractive index (we used $\lambda\nu = c_0/n$).

The spectral range ν_F being the difference in frequency between two neighbouring modes is then

$$\nu_F = \frac{c_0}{2nL}. \quad (2.73)$$

An example of the cavity modes structure can be observed in the next chapter in, in figure 3.1.

Chapter 3

Analysing tool

This part presents the Analysing Tool (AT) or algorithm which is intended to map the absorption spectrum inside a cavity with absorbing ions. We begin with an introduction which discusses the motivation of the method, followed by a derivation section, a discussion on some models or simulators for testing purposes and finally a result and discussion section.

3.1 Introduction

There should of course exist several potential solutions to the problem which this thesis treats, however all may not be able to meet the requirements a real application demands. These requirements include a reasonable accuracy with a runtime that's low enough to be practical during experiments. Also it cannot be too sensitive to noise and filtering, and should not require too large sample sizes.

The most direct approach is to choose some existing model which describes the system and try to invert the process, assuming that the absorption spectrum is the unknown and the output fields are the knowns. Depending on the method, this may either be impossible or too time-consuming for practical purposes.

The background for choosing the specific method in this report lies in Axel Thuresson's thesis [21]. In his thesis, two different models were developed for simulation of an OQM, with the purpose of investigating its efficiency. One of the models, referred to as a MB method, was of a more complicated nature, using Bloch theory [15] to take the light-matter interaction into account, meaning that one has to treat two equation systems at the same time, these being the Maxwell equations and Bloch equations.

However the other model, referred to as the interference model, is simpler, since it in essence treats the light-matter interaction using a simple dispersion model [19]. This means that one can ignore the time domain and treat the system in the frequency domain. Most importantly, the output transmitted and reflected fields can be calculated analytically, resulting in an easy implementation and fast runtime. Further this means that inverting the process is significantly easier than it would be using the other more complicated Maxwell-Bloch method.

The question then is, how does the two models compare to each other? In [21], the simulation output from the two models were shown to be quite

similar in shape and magnitude, however some discrepancy were observed. For example, when using the Maxwell-Bloch model, one encountered some notably strong oscillations in the transmission spectrum, which the author identified as a beating effect between between the readout pulse used and the radiation from the ions. However this doesn't necessarily mean that the other method isn't useful, rather one may just have to choose which readout pulse to use more carefully.

In the hope that the interference model is accurate enough for our purposes, we will in the next section derive an algorithm to map the absorption spectrum, using similar theory. In order to test algorithm, we will later borrow Axel's simulations and apply the algorithm to the output we receive, in order to test its performance.

3.2 Derivation

We begin by stating that all fields interacting with the absorbing medium are assumed to operate at such low strength, that we can assume that the Bloch equations will operate in the linear regime. This is of course something the operator in a real life experiment must take into consideration when he/she creates the interacting laser fields.

We will also initially assume that we have full knowledge of all outside fields¹. Further we also assume knowledge of any cavity or material parameters with arbitrary accuracy.

Finally we mention that the algorithm will come in two different versions. The approach is the same for both of them, they only differ in the final formula used to calculate the absorption. Any advantages or disadvantages with either of them will be investigated and discussed later on.

The cavity has length L , with reflection coefficients r_1 and r_2 at the left and right mirror respectively. Figure 2.3 still illustrates the system well.

3.2.1 Mirror interface matching

Using equations 2.60 and 2.66 derived in the theory section, we can assume that we can resolve the inside fields in the cavity with the same resolution as the outside field. Hence the field vectors inside the cavity is known at the mirror surfaces, which we denote

$$\mathbf{E}_1 = \begin{pmatrix} E_+(0, t) \\ E_-(0, t) \end{pmatrix} = \mathbf{E}(0, t), \quad (3.1)$$

$$\mathbf{E}_2 = \begin{pmatrix} E_+(L, t) \\ E_-(L, t) \end{pmatrix} = \mathbf{E}(L, t), \quad (3.2)$$

for mirror one and two respectively. They relate to the outside field as

$$\mathbf{E}_1 = \mathbf{T}_1 \begin{pmatrix} E_{inc} \\ E_{refl} \end{pmatrix}, \quad (3.3)$$

$$\mathbf{E}_2 = \mathbf{T}_2^{-1} \begin{pmatrix} E_{trans} \\ 0 \end{pmatrix}, \quad (3.4)$$

¹This not necessarily the case in an experimental setup, since detectors usually are limited to measuring intensity, not the phase of the electric field.

where E_{trans} , E_{refl} and E_{inc} are the outside transmitted, reflected and incoming field from the cavity.

3.2.2 The dispersion model

In the theory section we presented the Maxwell equation, which is assumed to be in the form

$$\frac{\partial^2 E}{\partial z^2} - \frac{1}{c_0^2} \frac{\partial^2 E}{\partial t^2} = \mu_0 \frac{\partial^2 P}{\partial t^2}. \quad (3.5)$$

We will now make the assumption that the material can be described with a simple dispersion model [19], with polarization being

$$P(z, t) = \epsilon \int_{-\infty}^{\infty} E(z, t - t') \chi(t') dt', \quad (3.6)$$

with $\chi(t)$ being the impulse response function of the material, more precisely the susceptibility of the material in the time domain. This assumption is in line with the fact that the Bloch equations are assumed to be in the linear regime.

We introduce the Fourier transform [25] defined by

$$\hat{f}(\omega) = \frac{1}{\sqrt{2\pi}} \int_{-\infty}^{\infty} f(t') e^{-\omega t'} dt', \quad (3.7)$$

with the inverse transform being

$$f(t) = \frac{1}{\sqrt{2\pi}} \int_{-\infty}^{\infty} \hat{f}(\omega') e^{-\omega' t} d\omega'. \quad (3.8)$$

Applying the Fourier transform on 3.5 and 3.6 result in

$$\frac{\partial^2 \hat{E}}{\partial z^2} + \frac{\omega^2 n^2}{c_0^2} \hat{E} = -\omega^2 \mu_0 \hat{P}, \quad (3.9)$$

and

$$\hat{P}(\omega) = \epsilon_0 \hat{\chi}(\omega) \hat{E}(\omega). \quad (3.10)$$

$\hat{\chi}$ is the frequency dependant susceptibility.

Combining the two equations above then yields the Helmholtz equation [19]

$$\frac{\partial^2 \hat{E}}{\partial z^2} + k(\omega)^2 \hat{E} = 0, \quad (3.11)$$

where $k(\omega)$ is the complex valued, frequency dependant wavenumber, given by

$$k(\omega) = \frac{\omega}{c_0} \sqrt{1 + \hat{\chi}}. \quad (3.12)$$

The aim of the review above was to show that the system in a dispersion model takes the form of a simple time independent second order partial differential equation. Since the equation is not differentiated along the frequency ω , we are allowed to solve the equation for each ω separately.

The solution to above equation is given by

$$\hat{E}(z, \omega) = \hat{\xi}_+(\omega) e^{-ik(\omega)z} + \hat{\xi}_-(\omega) e^{ik(\omega)z} + c.c., \quad (3.13)$$

where $\hat{\xi}_+$ and $\hat{\xi}_-$ depend only on ω and are determined at the boundaries.

We can write the wavenumber in real and imaginary part as

$$k(\omega) = \frac{n(\omega)\omega}{c_0} - i\frac{\alpha(\omega)}{2}, \quad (3.14)$$

where n is the refractive index and α is the absorption coefficient, defined so that the intensity of the electric field is attenuated along the z -axis as $|E_+(z)|^2 = |E_+(0)|^2 e^{-\alpha z}$. Comparing this expression to 3.12 reveals that the refractive index n and α depend non-linearly on $\hat{\chi}(\omega)$, however since it's the absorption coefficient which is the desired parameter, we can actually disregard $\hat{\chi}(\omega)$ and only use 3.14 as the expression for our wavenumber.

3.2.3 Final formulas

We conclude the derivation section by presenting two variants of the algorithm for the AT. Using 3.3 and 3.4 to calculate the fields at the boundaries inside the cavity and applying the fourier transform, we can use the dispersion model to compare the fields and determine how much of the fields have been absorbed as it propagates through the media.

Looking at the forward propagating components in 3.13 at mirror 1 and 2 we receive the following expression,

$$\hat{E}_+(L, \omega) = e^{-ik(\omega)L} \hat{E}_+(0, \omega) = \exp\left(-i\frac{n\omega_0}{L}\right) \exp\left(-\frac{\alpha L}{2}\right) \hat{E}_+(0, \omega), \quad (3.15)$$

Taking the absolute value over both sides and applying the natural logarithm allows us to extract the absorption coefficient, as

$$\alpha_1(\omega) = -\frac{2}{L} \log\left(\frac{|\hat{E}_+(L, \omega)|}{|\hat{E}_+(0, \omega)|}\right). \quad (3.16)$$

We use index 1 on α_1 to indicate that this is the first variant of the algorithm presented.

A alternative version can be constructed by instead comparing the forward and backward propagating field at the mirror 1. The backward field at left mirror is related to the field at mirror 2 in a similar way as in 3.15,

$$\hat{E}_-(0, \omega) = e^{ik(\omega)L} \hat{E}_-(L, \omega) = \exp\left(i\frac{n\omega_0}{L}\right) \exp\left(-\frac{\alpha L}{2}\right) \hat{E}_-(L, \omega). \quad (3.17)$$

Assuming no incoming fields from the right side of the cavity and using 2.64 in the cavity section to relate the backward field to the forward field at mirror 2, we have

$$\hat{E}_-(L, \omega) = r_2 \hat{E}_+(L, \omega). \quad (3.18)$$

Inserting into 3.17, and combining with 3.15 then result in

$$\begin{aligned} \hat{E}_-(0, \omega) &= \exp\left(i\frac{n\omega_0}{L}\right) \exp\left(-\frac{\alpha L}{2}\right) r_2 \exp\left(-i\frac{n\omega_0}{L}\right) \exp\left(-\frac{\alpha L}{2}\right) \hat{E}_+(0, \omega) \\ &= r_2 e^{-\alpha L} \hat{E}_+(0, \omega). \end{aligned} \quad (3.19)$$

In a similar way as in the case of formula 3.16 we now get

$$\alpha_2(\omega) = -\frac{1}{L} \log \left(\frac{|\hat{E}_-(0, \omega)|}{r_2 |\hat{E}_+(0, \omega)|} \right). \quad (3.20)$$

This is the second version of the algorithm, which we note doesn't require any knowledge of the fields at mirror 2, hence we only require the incoming and reflected light for this method.

3.2.4 Summary and comment on the algorithm

To summarize the algorithm.

1. Collect the outside fields, being E_{inc} , E_{refl} and E_{trans} . It's required that both the amplitude and phase of the fields are known, otherwise it's impossible to compute the inside cavity fields.
2. Use below formulas to calculate the inside fields \mathbf{E}_1 and \mathbf{E}_2 at the mirror 1 and 2.

$$\mathbf{E}_1 = \begin{pmatrix} E_+(0, t) \\ E_-(0, t) \end{pmatrix} = \frac{1}{t_1} \begin{pmatrix} 1 & r_1 \\ r_1 & 1 \end{pmatrix} \begin{pmatrix} E_{inc} \\ E_{refl} \end{pmatrix}, \quad (3.21)$$

$$\mathbf{E}_2 = \begin{pmatrix} E_+(L, t) \\ E_-(L, t) \end{pmatrix} = \frac{1}{t_2} \begin{pmatrix} 1 & r_2 \\ r_2 & 1 \end{pmatrix} \begin{pmatrix} E_{trans} \\ 0 \end{pmatrix}. \quad (3.22)$$

3. Apply the Fourier transform to \mathbf{E}_1 and \mathbf{E}_2 , which result in boundary fields $\hat{E}_+(0, \omega)$, $\hat{E}_-(0, \omega)$, $\hat{E}_+(L, \omega)$ and $\hat{E}_-(L, \omega)$.
4. Now use either the first method with formula

$$\textbf{Method 1 :} \quad \alpha_1(\omega) = -\frac{2}{L} \log \left(\frac{|\hat{E}_+(L, \omega)|}{|\hat{E}_+(0, \omega)|} \right) \quad (3.23)$$

or the second version with

$$\textbf{Method 2 :} \quad \alpha_2(\omega) = -\frac{1}{L} \log \left(\frac{|\hat{E}_-(0, \omega)|}{r_2 |\hat{E}_+(0, \omega)|} \right) \quad (3.24)$$

to receive the absorption spectrum.

Note that one can ignore the transmitted field when using the method 2, which may be more convenient and even give superior result in some cases.

Also note that in the first step it's not required that the *relative* phase of the incoming and transmitted field is known (it's okay if there is some unknown phase difference between these when measuring). This is because as seen in both 3.23 and 3.24, it's actually only the amplitude of of the inside fields which are required. However we still need the relative phase between incoming and reflected light, since it's otherwise impossible to determine fields $\hat{E}_+(0, \omega)$, $\hat{E}_-(0, \omega)$ at mirror 1.

The big concern now is how suitable and accurate the algorithm actually is, or if it is of any practical use at all. After all it doesn't take into account the Bloch equations. Below we will present some models and simulations which will be used to test the algorithm.

3.3 Models for testing

The simulators used in this section, which were discussed briefly in the introduction of this part, were all developed by Axel Thuresson for his master's thesis [21]. The first simulator uses what we refer to as an interference model, while the second uses a Maxwell-Bloch (MB) model. A short description of each is in order, however one should mention that the original purpose of these simulators were different than that of ours, hence they may not be suited for our purposes. They were intended to simulate the storage efficiency of the cavity, for which you only require the intensities of the fields. However our algorithm requires the phases of the fields.

3.3.1 Interference model

The interference assumes a simple dispersion model as presented above, with wavenumber

$$k = \frac{\omega}{c_0} (n_r(\omega) + in_i(\omega)). \quad (3.25)$$

We are mostly interested in the imaginary part n_i , which relates to the absorption as $\alpha = -2\omega n_i(\omega)/c_0$ [19]. The electric field is represented as

$$E(\omega, t, z) = E_0(\omega)e^{i\omega t}e^{-ik(\omega)z}, \quad (3.26)$$

which is convenient to treat analytically.

The fields of interest are the reflected and the transmitted. These can be derived by letting the field for each frequency, bounce an infinitely number of times inside the cavity, and sum up all the outgoing field components. For the transmitted field we get

$$\begin{aligned} E_{trans}(\omega) &= E(\omega, t, L)t_1t_2 + E(\omega, t, 3L)t_1r_2r_1t_2 + \dots = \\ &= E_0t_1t_2e^{i\omega t+ikL} \sum_{n=0}^{\infty} (e^{i2kL}(r_1r_2)^n) \\ &= \frac{E_0e^{i\omega t+ikL}t_1t_2}{1 - r_1r_2e^{i2kL}}. \end{aligned}$$

The first term in the upper row is the part which have passed through mirror one and two (hence multiplication by t_1 and t_2) and propagated one cavity length L , the second which have bounced on both the mirrors and travelled one extra round trip in the cavity and so forth. The last step is due to the formula being a simple geometrical sum.

The same treatment for the reflected field result in

$$\begin{aligned} E_{refl}(\omega) &= -E(\omega, t, 0)r_1 + E(\omega, t, 2L)t_1r_2t_1 + E(\omega, t, 4L)t_1r_2r_1r_2t_1\dots \\ &= E_0e^{i\omega t} \left(-r_1 + \frac{t_1^2r_2e^{i2kL}}{1 - r_1r_2e^{i2kL}} \right). \end{aligned}$$

The first term is the direct reflection of the incoming field at mirror 1, while the second is the component which has been reflected at mirror 2.

These formulas can now be used to calculate the output fields from the cavity. The transmission and reflection is calculated by

$$R(\omega) = \left| \frac{E_{refl}(\omega)}{E_0(\omega)} \right|^2 = \left| -r_1 + \frac{t_1^2 r_2 e^{i2kL}}{1 - r_1 r_2 e^{i2kL}} \right|^2, \quad (3.27)$$

$$T(\omega) = \left| \frac{E_{trans}(\omega)}{E_0(\omega)} \right|^2 = \left| \frac{t_1 t_2}{1 - r_1 r_2 e^{i2kL}} \right|^2. \quad (3.28)$$

3.3.2 Maxwell-Bloch model

The second model differs in the sense that here we actually make use of the Bloch equations to model the light-matter interaction. This model becomes possible to treat numerically by making the assumption that both the electric field and polarization can be represented by

$$E(z, t) = \sum_n E_n(t) u_n(z), \quad (3.29)$$

$$P(z, t) = \sum_n P_n(t) u_n(z), \quad (3.30)$$

where $u_n(z)$ are the eigenmodes of a cold cavity, which are the solution to the Laplace equation

$$\frac{\partial u_n}{\partial t} + k_n^2 u_n = 0, \quad (3.31)$$

$$u_n(0) = 0, \quad (3.32)$$

$$u_n(L) = 0, \quad (3.32)$$

where $k_n = \omega_n n/c$ and with solutions

$$u_n(z) = \sin\left(\frac{\pi n z}{L}\right). \quad (3.33)$$

Hence we use the eigenmodes of the cavity as a basis for the total field. This makes the calculations considerably easier, since it's possible to extract the spatially dependant part of the equations, when inserting the fields above into the Maxwell equation.

However there are several problems with this assumption, for example any spatial dependency in the Bloch equations are no longer taken into account, and also while the amplitude of the fields may be calculated accurately, the same cannot be said for the phase. Since the phase is absolutely essential for our analysing algorithm, this model is probably not suited for our purposes.

In [21] Axel showed that both simulators gave similar output when looking at the transmission intensity spectrum, although there were some discrepancy. The interference model can't for example model effects such as slow light.

3.4 Results

Here we present results from some simulations assuming a predefined absorption profile. The procedure is the one presented in figure 1.5. For each simulation

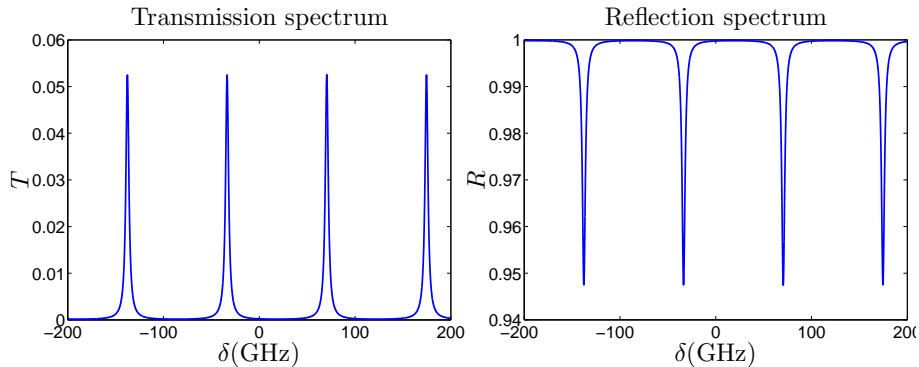


Figure 3.1: Transmission and reflection spectrum from a cold cavity.

we will utilize the AT algorithm derived in subsection 3.2.4 to get a calculated absorption spectrum, which will then be compared to the original absorption. The interference model is investigated first.

Also note that it's a convention in quantum optics to present the absorption using coefficient $\alpha_L = \alpha L$. In this report we will use fairly low values of up to 3.

3.4.1 Interference model

We begin by showing some features of the output from the interference simulator. In this section we only look at the field as a function of detuning, since the interference simulator only treats the fields in the frequency domain. We note that the laser frequency will for the entirety of this report be set to $f_L = \omega_L/(2\pi) = 500$ THz. As a reminder, note that this value in most cases is irrelevant, since we actually are looking at the detuning difference $\delta = \omega - \omega_L$, and not the absolute frequency ω .

The cavity length is chosen to 0.800 mm, however this value will be varied slightly later in order to see how the transmission is affected. Cavity mirrors are always set to $R_1 = 0.800$ and $R_2 = 0.997$ for mirror 1 and 2 respectively, further the host or crystal medium refractive index is set to $n_{host} = 1.8$.

Cold Cavity

In figure 3.1 we see the simulated transmission and reflection spectrum from a cold cavity (a cavity with no absorbing medium). We note that the free spectral range (distance between the peaks) is 104.09 GHz, which is what you get with equation 2.73 in the cavity theory section.

Absorbing ions introduced

We now introduce the absorbing ions into our system. In figure 3.5 we see the chosen absorption spectrum, which consist of two side walls and six AFC peaks. Note that the region in detuning is in the Mhz range, while the previous figure were in the GHz range. Also, in this particular case we assume that α_L continues outside the graph with the same strength of $\alpha_L = 3$.

The motivation for the chosen profile is that it provides both some fine structures as well as some region with a relatively high absorption, so it should be easy to analyze both the resolution and discrepancy. Hence we will use this shape throughout the report, though the strength may vary.

In figure 3.2 we see the transmission and reflection spectrum from the cavity with the absorption spectrum applied, with same cavity parameters as before, with cavity length $L = 0.800$ mm as in the first case. The frequency range is in the GHz range in order to compare with previous case. It's apparent that a sharp transmission line has appeared over in the center of the spectra, where we have placed our absorbing ions.

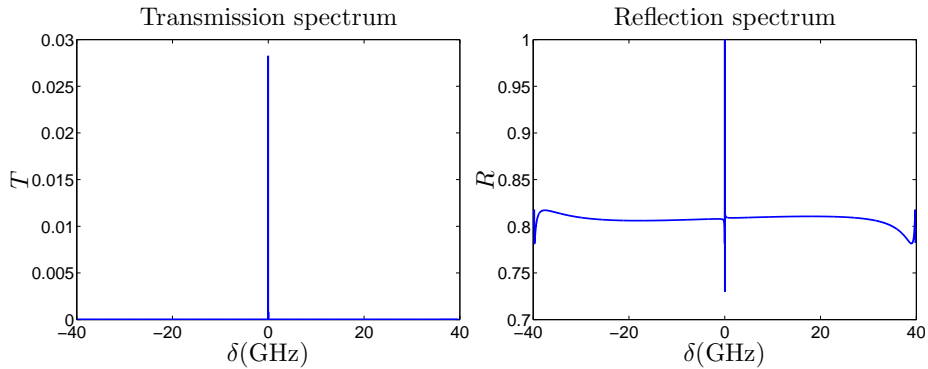


Figure 3.2: Transmission and reflection spectrum from a cavity with absorbing ions.

To help us understand this result, we look at figure 3.3 which displays the calculated real-valued refractive index using the Kramer-Krönig relations [19]. These relate the refractive index to the absorption spectrum, which shows that the refractive index is proportional to the derivative of the absorption with respect to frequency, meaning that we should see some resulting changes in refractive index over the absorbing region.

This is apparent when looking at the central region where there is a significant spike change. Since the cavity modes as seen in the cavity section are dependant on the refractive index, it's reasonable that we should get some transmission lines in this region.

Applying the analysing tool

It's now time to actually apply our algorithm on our output data. In figure 3.4, the reflection and transmission spectrum is shown, with the detuning range being in the MHz range. The parameters are still the same otherwise.

Applying both versions of our algorithm derived subsection 3.2.4 on the data in figure 3.4, we end up with the absorption spectra shown in figure 3.5, with the original spectrum included for comparison. It's apparent that both versions of the algorithm produces profiles nearly identical to the original spectrum. The relative error between the computed and original profile for both algorithm versions has been measured to be well below the order 10^{-10} , so we can conclude that profiles for all practical purposes are identical.

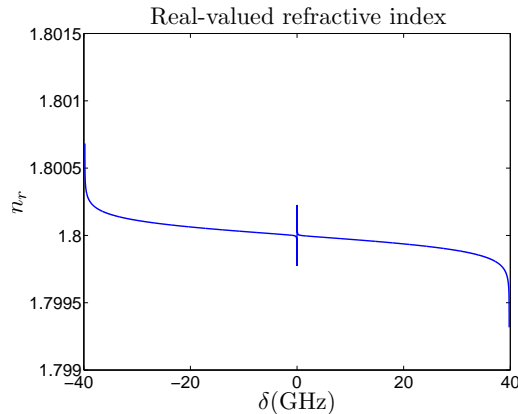


Figure 3.3: The real-valued refractive index, as a function of frequency.

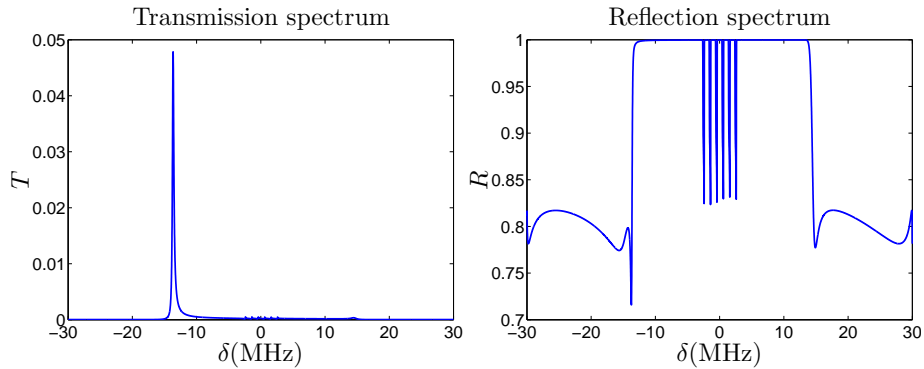


Figure 3.4: Transmission and reflection spectrum from a cavity with absorbing ions. Length is $L = 8$ mm and reflection coefficients are $R_1 = 0.800$ and $R_2 = 0.997$.

Some additional cases

It's of interest to present some additional cases where we have placed the cavity mode in different positions in the spectrum. The motivation for this is that it's of interest to see if this affect the AT results. This is also a request from the experimentalists in the QI-group, who desires to see how the different transmission look for different cavity modes.

The modes are shifted by slightly changing the cavity length in the simulation. Four cases are being presented with cavity lengths as shown in table 3.1. In figure 3.6 to 3.9, we plot the output spectra for different cases, where we can see how the transmission is gradually changed. We note that for each figure we plot the case where we only have an empty well profile, and the case with AFC peaks included, for comparison.

Applying the algorithm at each of these cases, result in equally good computed profile, as was the case in figure 3.5, hence there is no meaning in plotting these profiles. We note that a wide arrange of different cavity lengths, not displayed here, have been tested which all provided the same good result concerning

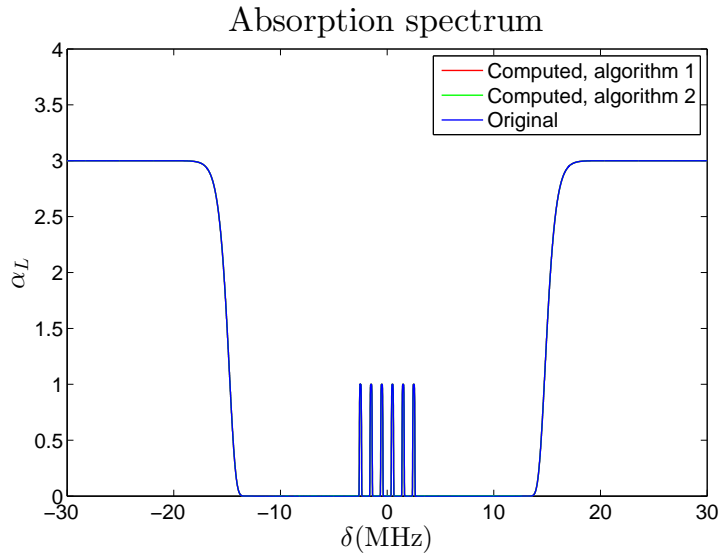


Figure 3.5: Absorption spectrum, represented using $\alpha_L = \alpha(\omega)L$, as a function of detuning. It includes the computed profiles using both the first and second version of the algorithm, with original profile for comparison as well. Since they overlap each other, we only see one of the lines. Also note that the lines continue with the same value of $\alpha_L = 3$ outside the graph (only in this particular case).

Table 3.1: Cavity lengths for each investigated case.

Case	L
1	0.79999420 mm
2	0.7999622 mm
3	0.7999462 mm
4	0.8000262 mm

the computed absorption profiles.

3.4.2 Maxwell-Bloch model

As already mentioned above, the Maxwell-Bloch simulator is predicted to be unsuitable for testing the algorithm. We use the same parameters as before, with $L = 0.8$ mm, $R_1 = 0.800$ and $R_2 = 0.997$. Also the absorption spectrum is the same as before. In figure 3.10 we have plotted the intensity of the incoming, reflected and transmitted field, as a function of the time. The incoming field is a Supergaussian shaped frequency chirped pulse, meaning that the frequency is increasing linearly with time (the input field is explained more in section 4.3.1, further down in the next chapter).

In figure 3.11 we see the absorption spectrum when applying our algorithm on the output. It's very clear that our method result in very large discrepancies in the spectrum. However we can still see features such as the AFC- peaks. It should however be clear that our algorithm is either not well enough suited for

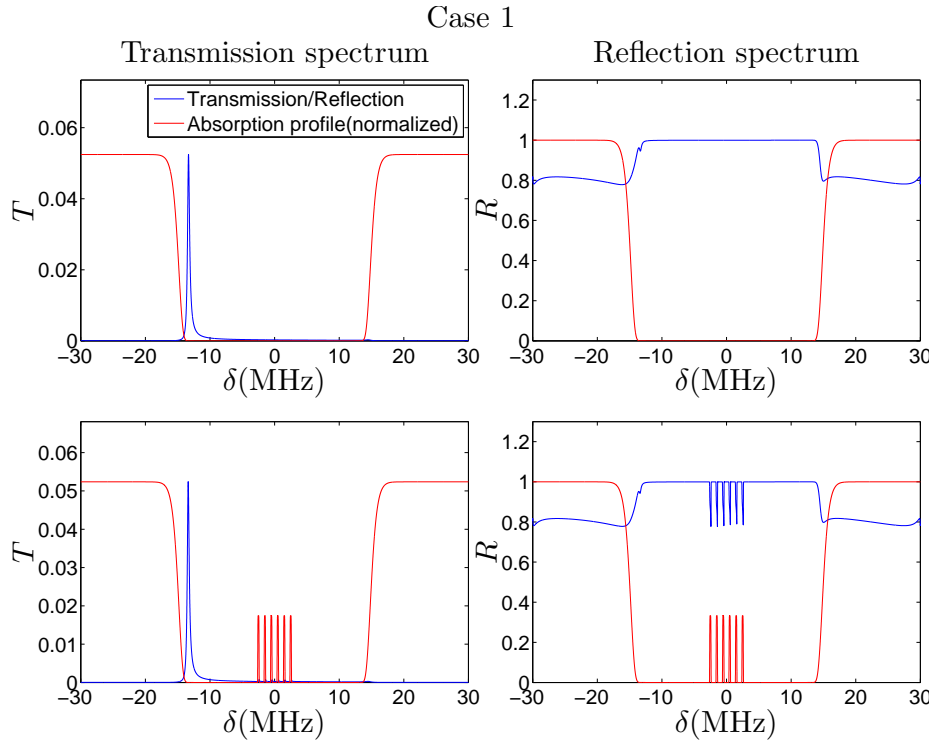


Figure 3.6: Transmission and reflection lines versus absorption profile. In the upper two graphs we have excluded the AFC peaks, while they have been included in the lower graphs.

the problem, or that it is the simulator which is not suited for testing.

3.5 Discussion

Our algorithm were shown to perform well when applied to the interference model, but this is not surprising or unreasonable, since they are based on the same theory and assumptions. The question still remains in how well it performs when the simulations are based on a more advanced model.

The test with the Maxwell-Bloch simulator in the section above from [21] did not provide any conclusions regarding the performance on the algorithm. It only confirmed the unsuitability of the specific model for our purpose. The problem may depend on the fact that the spacial dependence of the electric fields are lost when we express the fields with the eigenmodes as a basis. While we may receive good values for the intensities of the fields, we loose the phase, which is essential to our algorithm.

The problem discussed here thus raises the need for a simulator which preserves the spacial phase of the field. The next chapter is dedicated to this problem.

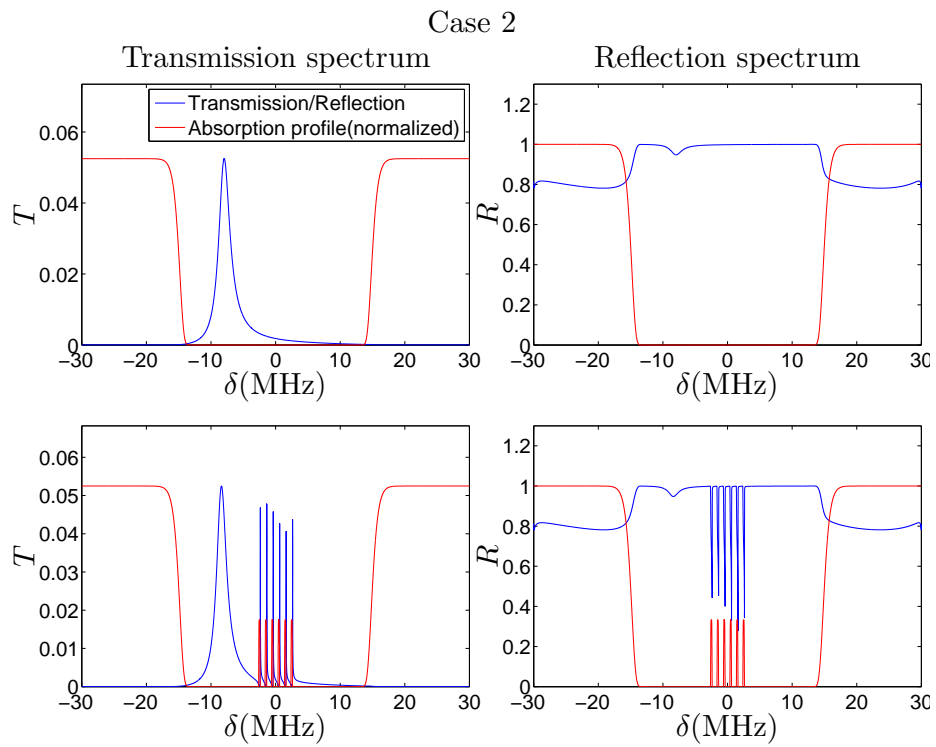


Figure 3.7: Transmission and reflection lines versus absorption profile. In the upper two graphs we have excluded the AFC peaks, while they have been included in the lower graphs.

Case 3

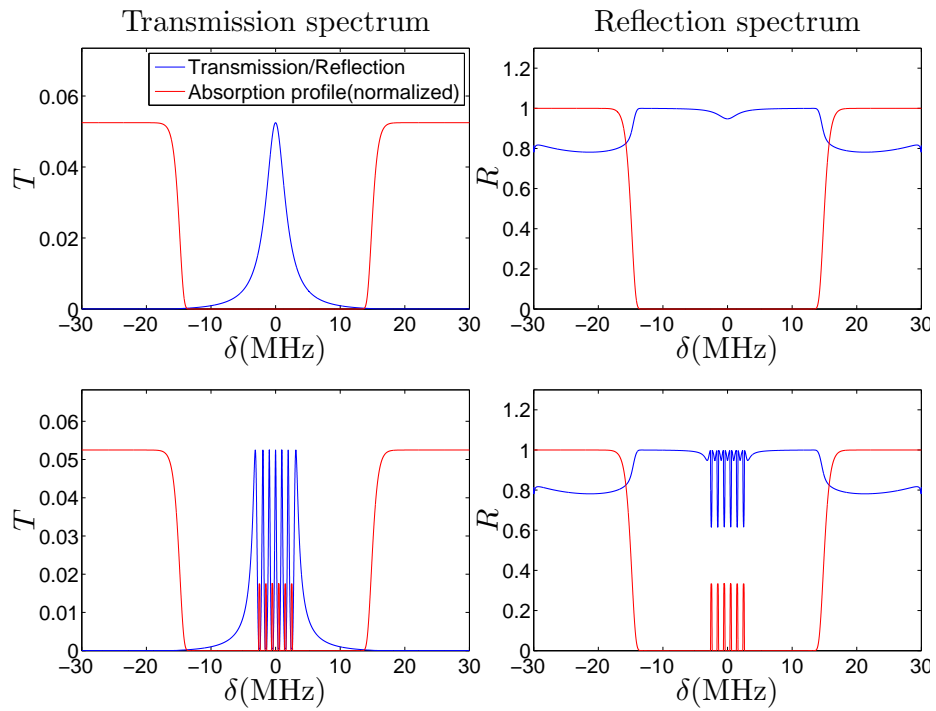


Figure 3.8: Transmission and reflection lines versus absorption profile. In the upper two graphs we have excluded the AFC peaks, while they have been included in the lower graphs.

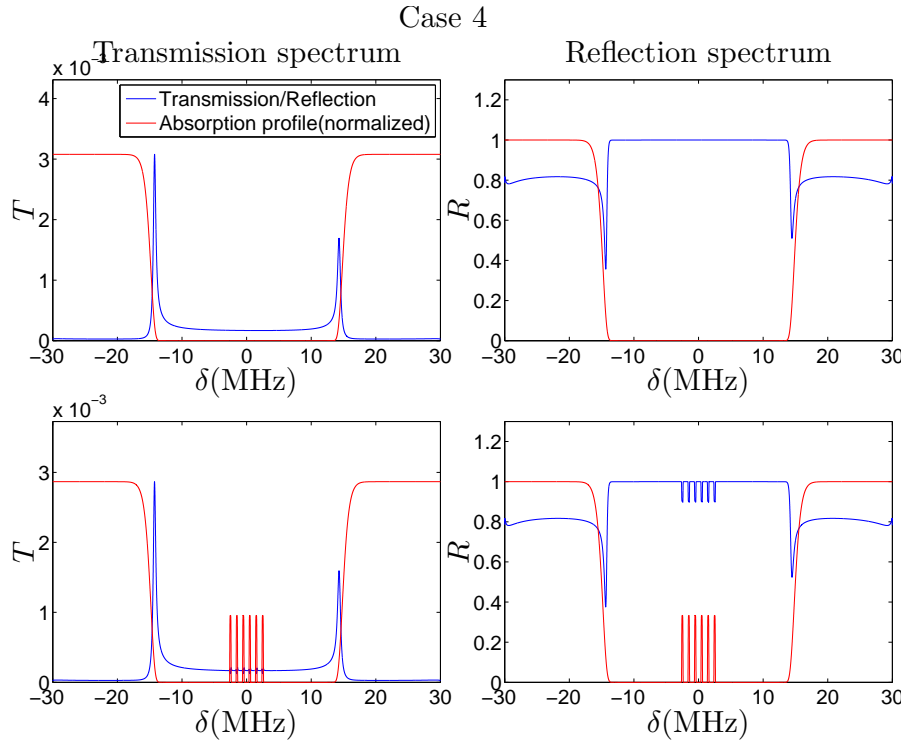


Figure 3.9: Transmission and reflection lines versus absorption profile. In the upper two graphs we have excluded the AFC peaks, while they have been included in the lower graphs.

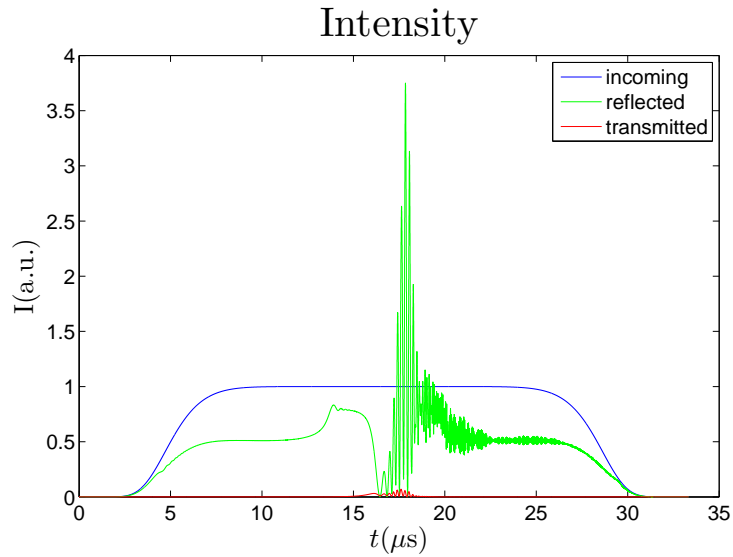


Figure 3.10: Intensity of the incoming, reflected and transmitted field, as a function of time. Parameters are $L = 0.8$ mm, $R_1 = 0.800$ and $R_2 = 0.997$.

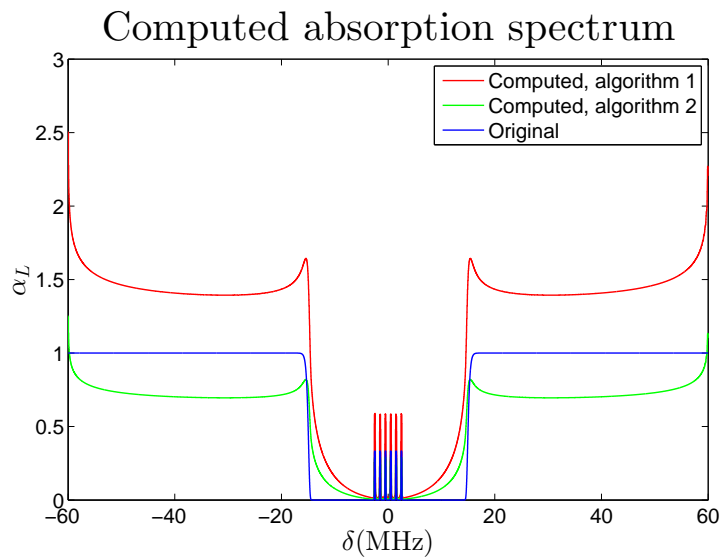


Figure 3.11: Absorption spectrum using the MB simulator. The absorption is expressed using $\alpha_L = \alpha(\omega)L$, as a function of detuning. It includes the computed profiles using both the first and second version of the algorithm, with original profile for comparison aswell.

Chapter 4

Maxwell-Bloch simulator

In the previous chapter we observed that there is a need for a MB simulator more suited for our own purpose, to confirm that our Analysing Tool (AT) or algorithm can handle a more complicated model. The assumption that the electric field can be expressed in a basis of the cavity eigen modes is often times a good one (more on this topic in [20]), however it will be avoided here, since we need to ensure that both the phase and amplitude of the wave is computed accurately.

We begin by deriving the complete set of Maxwell-Bloch equations, following up with the discretization of the method and conclude with a result and discussion part.

4.1 Derivation

The model will be based on the Bloch equations and Maxwell equations already presented in the theory section. We begin by combining the theory into a complete set of equations, which will then be discretized in order to solve them numerically.

4.1.1 Maxwell-Bloch equations

A representation of the equations is in order. The electric field is represented in its full form as

$$\begin{aligned} E(z, t) = & \xi_+(z, t) \cos(\omega_L t - k_L z + \varphi_+(t)) + \dots \\ & \xi_-(z, t) \cos(\omega_L t + k_L z + \varphi_-(t)) \end{aligned} \quad (4.1)$$

and is in the cavity medium described by the Maxwell equation

$$\frac{\partial^2 E}{\partial z^2} - \frac{n^2}{c_0^2} \frac{\partial^2 E}{\partial t^2} = \mu_0 \frac{\partial^2 P}{\partial t^2}. \quad (4.2)$$

The polarization is described by

$$P(z, t) = \frac{N}{2\pi V} \int_{-\infty}^{\infty} g(\delta) p_x(z, t, \delta) d\delta, \quad (4.3)$$

where $g(\omega)$ is the normalized absorption profile and p_x the macroscopic dipole moment. Also remember that $k_L = \omega_L n / c_0$.

In the first section of the theory part, we introduced some terminology regarding the electric fields. This will be used to show that we can separate the forward and backward field components and more importantly remove the rapidly oscillating parts from the equations. This serve to make our problem more manageable numerically. The field could be written in the form

$$E(z, t) = \frac{1}{2} \{ \mathbf{e}^T \mathbf{E} e^{i\omega_L t} + c.c. \}, \quad (4.4)$$

where

$$\mathbf{e} = \mathbf{e}(z, t) = \begin{pmatrix} e^{-ik_L z} \\ e^{ik_L z} \end{pmatrix} \quad (4.5)$$

and the field vector were determined to be

$$\mathbf{E} = \begin{pmatrix} \mathcal{E}_+(z, t) \\ \mathcal{E}_-(z, t) \end{pmatrix}, \quad (4.6)$$

$$\mathcal{E}_+ = \xi_+(z, t) e^{i\varphi_+(t)}, \quad (4.7)$$

$$\mathcal{E}_- = \xi_-(z, t) e^{i\varphi_-(t)}. \quad (4.8)$$

As a reminder, c.c. stands for the complex conjugate term.

Bloch equations

In theory chapter, we derived the Bloch equations assuming an electric field in the form

$$E(z, t) = \xi(z, t) e^{i\varphi(t)} e^{i\omega_L t} + \xi(z, t)^* e^{-i\varphi(t)} e^{-i\omega_L t}. \quad (4.9)$$

In our system however it's necessary to treat the field using the expanded vector form in 4.4. Hence we introduce the Rabi frequency in vector form $\mathbf{\Omega}$, such that

$$\mathbf{\Omega} = \mathbf{e}^T \mathbf{\Omega} = \frac{\mu_{ge} \mathbf{e}^T \mathbf{E}}{\hbar} = \frac{\mu_{ge}}{\hbar} \left[\xi_+(z, t) e^{i\varphi_+(t)} + \xi_-(z, t) e^{i\varphi_-(t)} \right], \quad (4.10)$$

where

$$\mathbf{\Omega} = \begin{pmatrix} \Omega_+(z, t) \\ \Omega_-(z, t) \end{pmatrix} = \frac{\mu_{ge}}{\hbar} \begin{pmatrix} \xi_+(z, t) e^{i\varphi_+(t)} \\ \xi_-(z, t) e^{i\varphi_-(t)} \end{pmatrix} \quad (4.11)$$

The electric field can now be written

$$E(z, t) = \frac{\hbar}{2\mu_{ge}} \{ \mathbf{e}^T \mathbf{\Omega} e^{i\omega_L t} + \mathbf{e}^\dagger \mathbf{\Omega}^* e^{-i\omega_L t} \}. \quad (4.12)$$

Since the dipole moment p_x in the Maxwell equation is a function of the Bloch components u and v it's necessary to expand these as well, as

$$u = \mathbf{e}^T \mathbf{u}, \quad (4.13)$$

$$v = \mathbf{e}^T \mathbf{v}, \quad (4.14)$$

where

$$\mathbf{u} = \begin{pmatrix} u_+(z, t, \delta) \\ u_-(z, t, \delta) \end{pmatrix}, \quad (4.15)$$

$$\mathbf{v} = \begin{pmatrix} v_+(z, t, \delta) \\ v_-(z, t, \delta) \end{pmatrix}. \quad (4.16)$$

The dipole moment then turns into

$$p_x(z, t, \delta) = \frac{\mu_{ge}}{2} \{ \mathbf{e}^T(\mathbf{u} + i\mathbf{v})e^{i\omega_L t} + \mathbf{e}^\dagger(\mathbf{u} - i\mathbf{v})e^{-i\omega_L t} \}. \quad (4.17)$$

The Bloch equations were derived in the theory section at 2.53, however we need to reformulate the equation by representing the Bloch components \mathbf{u} and \mathbf{v} .

Using $u = \mathbf{e}^T \mathbf{u}$, $v = \mathbf{e}^T \mathbf{v}$ and $\Omega = \mathbf{e}^T \mathbf{\Omega}$, we can expand \mathbf{A} so that it relates to u_+ , u_- , v_+ , v_- and w instead. Inserting \mathbf{u} and \mathbf{b} into equation 2.53, result in the modified equation

$$\dot{\mathbf{R}} = \mathbf{A}\mathbf{R} + \boldsymbol{\varphi} + \boldsymbol{\xi}, \quad (4.18)$$

where

$$\mathbf{A} = \begin{pmatrix} -\frac{\Gamma}{2} & 0 & -\delta & 0 & \frac{i}{2}(\Omega_+ - \Omega_-^*) \\ 0 & -\frac{\Gamma}{2} & 0 & -\delta & \frac{i}{2}(\Omega_- - \Omega_+^*) \\ \delta & 0 & -\frac{\Gamma}{2} & 0 & \frac{i}{2}(\Omega_+ + \Omega_-^*) \\ 0 & \delta & 0 & -\frac{\Gamma}{2} & \frac{i}{2}(\Omega_- + \Omega_+^*) \\ -\frac{i}{2}(\Omega_+ - \Omega_-^*) & \frac{i}{2}(\Omega_- - \Omega_+^*) & -\frac{1}{2}(\Omega_+ + \Omega_-^*) & -\frac{1}{2}(\Omega_- + \Omega_+^*) & -\Gamma \end{pmatrix}. \quad (4.19)$$

Bloch vector

$$\mathbf{R} = \begin{pmatrix} u_+ \\ u_- \\ v_+ \\ v_- \\ w \end{pmatrix}, \quad (4.20)$$

constant vector

$$\boldsymbol{\varphi} = \begin{pmatrix} 0 \\ 0 \\ 0 \\ 0 \\ \Gamma \end{pmatrix} \quad (4.21)$$

and rest term

$$\boldsymbol{\xi} = \begin{pmatrix} 0 \\ 0 \\ 0 \\ 0 \\ \xi \end{pmatrix} \quad (4.22)$$

ξ is a rest term which consist of terms e^{-i2kz} , e^{i2kz} , u and v . The rest term is annoying since it contains rapidly oscillating terms (e^{-i2kz}), which we can't extract or remove mathematically. We can only make the assumption that it can be neglected.

We motivate this by assuming that all interacting fields will be relatively weak, making this term relatively small compared to w , which will be close to unity as most ions won't be excited in the sample.

Maxwell part

For convenience we will express the field using the Rabi frequency Ω , since the connection to the Bloch equations becomes more clear. From 4.12 we already

have

$$E(z, t) = \frac{\hbar}{2\mu_{ge}} \{ \mathbf{e}^T \mathbf{\Omega} e^{i\omega_L t} + c.c. \}. \quad (4.23)$$

Inserting this into the Maxwell equation in 4.2 result in

$$\begin{aligned} \frac{\hbar}{2\mu_{ge}} \left[\frac{\partial^2 \mathbf{e}^T \mathbf{\Omega} e^{i\omega_L t}}{\partial z^2} - \frac{n^2}{c_0^2} \frac{\partial^2 \mathbf{e}^T \mathbf{\Omega} e^{i\omega_L t}}{\partial t^2} + c.c. \right] &= \mu_0 \frac{\partial^2 P}{\partial t^2} \\ \iff \\ \frac{\partial^2 \mathbf{e}^T \mathbf{\Omega} e^{i\omega_L t}}{\partial z^2} - \frac{n^2}{c_0^2} \frac{\partial^2 \mathbf{e}^T \mathbf{\Omega} e^{i\omega_L t}}{\partial t^2} + c.c. &= \frac{2\mu_0 \mu_{ge}}{\hbar} \frac{\partial^2 P}{\partial t^2}. \end{aligned} \quad (4.24)$$

Before we make any further derivations, we note we have the following expressions for the derivatives of the propagation matrices \mathbf{e}

$$\begin{aligned} \frac{\partial \mathbf{e}^T e^{i\omega_L t}}{\partial z} &= \frac{i\omega_L n}{c_0} \mathbf{e}^T e^{i\omega_L t} \begin{pmatrix} -1 & 0 \\ 0 & 1 \end{pmatrix}, \\ \frac{\partial^2 \mathbf{e}^T e^{i\omega_L t}}{\partial z^2} &= -\frac{\omega_L^2 n^2}{c_0^2} \mathbf{e}^T e^{i\omega_L t}, \\ \frac{\partial \mathbf{e}^T e^{i\omega_L t}}{\partial t} &= i\omega_L \mathbf{e}^T e^{i\omega_L t}, \\ \frac{\partial^2 \mathbf{e}^T e^{i\omega_L t}}{\partial t^2} &= -\omega_L^2 \mathbf{e}^T e^{i\omega_L t}. \end{aligned} \quad (4.25)$$

The left part in 4.24 then expands into

$$\begin{aligned} &\mathbf{e}^T e^{i\omega_L t} \left[-\frac{\omega_L^2 n^2}{c_0^2} \mathbf{\Omega} + i2 \frac{\omega_L n}{c_0} \begin{pmatrix} -1 & 0 \\ 0 & 1 \end{pmatrix} \frac{\partial \mathbf{\Omega}}{\partial z} + \frac{\partial^2 \mathbf{\Omega}}{\partial z^2} + c.c. \right] + \dots \\ &- \frac{n^2}{c_0^2} \mathbf{e}^T e^{i\omega_L t} \left[-\omega_L^2 \mathbf{\Omega} + i2\omega_L \frac{\partial \mathbf{\Omega}}{\partial t} + \frac{\partial^2 \mathbf{\Omega}}{\partial t^2} + c.c. \right] = \\ &= \mathbf{e}^T e^{i\omega_L t} \left[i2 \frac{\omega_L n}{c_0} \begin{pmatrix} -1 & 0 \\ 0 & 1 \end{pmatrix} \frac{\partial \mathbf{\Omega}}{\partial z} + \frac{\partial^2 \mathbf{\Omega}}{\partial z^2} - i2 \frac{\omega_L n^2}{c_0^2} \frac{\partial \mathbf{\Omega}}{\partial t} - \frac{n^2}{c_0^2} \frac{\partial^2 \mathbf{\Omega}}{\partial t^2} + c.c. \right]. \end{aligned}$$

To simplify the equations we apply the so called *slowly varying envelope approximation* [23, 20], which is based on the assumption that the envelope of the function is varying very slowly compared to the fast oscillating term, in this case \mathbf{e}^T and $e^{i\omega_L t}$. Since ω_L is in the THz range and the spectra we are looking at is in the MHz range, this is an acceptable assumption. The approximation then states that

$$\begin{aligned} \frac{\partial^2 \mathbf{\Omega}}{\partial z^2} &\ll \frac{\omega_L n}{c_0} \frac{\partial \mathbf{\Omega}}{\partial z} \ll \frac{\omega_L^2 n^2}{c_0^2} \mathbf{\Omega}, \\ \frac{\partial^2 \mathbf{\Omega}}{\partial t^2} &\ll \omega_L \frac{\partial \mathbf{\Omega}}{\partial t} \ll \omega_L^2 \mathbf{\Omega}. \end{aligned}$$

Hence we are allowed to throw away the second derivatives in the Maxwell equation above resulting in

$$\mathbf{e}^T e^{i\omega_L t} \left[i2 \frac{\omega_L n}{c_0} \begin{pmatrix} -1 & 0 \\ 0 & 1 \end{pmatrix} \frac{\partial \mathbf{\Omega}}{\partial z} - i2 \frac{\omega_L n^2}{c_0^2} \frac{\partial \mathbf{\Omega}}{\partial t} + c.c. \right] = \frac{2\mu_0 \mu_{ge}}{\hbar} \frac{\partial^2 P}{\partial t^2}. \quad (4.26)$$

The next step is to expand the polarization part in the right part of the equation. In the theory part, at 2.37 in we assumed that the dipole moment could be expressed as

$$p_x(z, t, \delta) = \frac{\mu_{ge}}{2} \{ \mathbf{e}^T(\mathbf{u} + i\mathbf{v})e^{i\omega_L t} + c.c. \}. \quad (4.27)$$

Inserting 4.3 and above into the right part of 4.26 and expanding the derivative result in

$$\begin{aligned} \frac{2\mu_0\mu_{ge}}{\hbar} \frac{\partial^2 P}{\partial t^2} &= \frac{2\mu_0\mu_{ge}^2 N}{2\pi\hbar V} \frac{\partial^2}{\partial t^2} \int_{-\infty}^{\infty} g(\delta) \{ \mathbf{e}^T(\mathbf{u} + i\mathbf{v})e^{i\omega_L t} + c.c. \} d\delta \\ &= \frac{\mu_0\mu_{ge}^2 N}{2\pi\hbar V} \mathbf{e}^T e^{i\omega_L t} \int_{-\infty}^{\infty} g(\delta) \{ \dots \\ &\quad -\omega_L^2(\mathbf{u} + i\mathbf{v}) + i\omega_L \frac{\partial}{\partial t}(\mathbf{u} + i\mathbf{v}) + \frac{\partial^2}{\partial t^2}(\mathbf{u} + i\mathbf{v}) + c.c. \} d\delta. \end{aligned} \quad (4.28)$$

Once again we apply the slowly varying envelope approximation (with the assumption that \mathbf{u} and \mathbf{v} varies slowly compared to ω_L), with inequalities

$$\frac{\partial^2(\mathbf{u} + i\mathbf{v})}{\partial t^2} \ll \omega_L \frac{\partial(\mathbf{u} + i\mathbf{v})}{\partial t} \ll \omega_L^2(\mathbf{u} + i\mathbf{v}). \quad (4.29)$$

In the equation above we can then remove both derivatives, resulting in

$$\frac{2\mu_0\mu_{ge}}{\hbar} \frac{\partial^2 P}{\partial t^2} = -\frac{\mu_0\mu_{ge}^2 N}{2\pi\hbar V} \mathbf{e}^T e^{i\omega_L t} \int_{-\infty}^{\infty} g(\delta) \{ (\mathbf{u} + i\mathbf{v}) + c.c. \} d\delta.$$

Inserting into 4.26 gives

$$\begin{aligned} i2 \frac{\omega_L n}{c_0} \begin{pmatrix} -1 & 0 \\ 0 & 1 \end{pmatrix} \frac{\partial \mathbf{\Omega}}{\partial z} - i2 \frac{\omega_L n^2}{c_0^2} \frac{\partial \mathbf{\Omega}}{\partial t} = \\ -\frac{\omega_L^2 \mu_0 \mu_{ge}^2 N}{2\pi \hbar V} \int_{-\infty}^{\infty} g(\delta) \{ (\mathbf{u} + i\mathbf{v}) \} d\delta, \end{aligned}$$

where we have extracted $\mathbf{e}^T e^{i\omega_L t}$ and dropped the complex conjugate terms. Further rearranging yields

$$\begin{aligned} \begin{pmatrix} -1 & 0 \\ 0 & 1 \end{pmatrix} \frac{\partial \mathbf{\Omega}}{\partial z} - \frac{n}{c_0} \frac{\partial \mathbf{\Omega}}{\partial t} &= i \frac{\omega_L c_0 \mu_0 \mu_{ge}^2 N}{4\pi n \hbar V} \int_{-\infty}^{\infty} g(\delta) \{ (\mathbf{u} + i\mathbf{v}) \} d\delta \\ &= \frac{i}{2\pi} \int_{-\infty}^{\infty} \alpha(\delta) \{ (\mathbf{u} + i\mathbf{v}) \} d\delta, \end{aligned} \quad (4.30)$$

where α is the absorption coefficient, with

$$\alpha(\delta) = \frac{\omega_L c_0 \mu_0 \mu_{ge}^2 N}{2\pi n \hbar V} g(\delta). \quad (4.31)$$

The motivation for this formula can be found in [15].

Boundary conditions

The boundary conditions depends on the incoming field and the mirrors. At the left mirror, we can use 2.57 to relate the forward to the backward propagating field

$$E_+(0, t) = t_1 E_{inc} + r_1 E_-(0, t). \quad (4.32)$$

Expressing the fields in their Rabi frequencies as

$$E_+(0, t) = \frac{\hbar}{2\mu_{ge}} \Omega_+(0, t) e^{-ik_L 0} e^{i\omega_L t} + c.c., \quad (4.33)$$

$$E_-(0, t) = \frac{\hbar}{2\mu_{ge}} \Omega_-(0, t) e^{ik_L 0} e^{i\omega_L t} + c.c., \quad (4.34)$$

$$E_{inc} = \frac{\hbar}{2\mu_{ge}} \Omega_{inc}(t) e^{i\omega_L t} + c.c. \quad (4.35)$$

and inserting in above, result in

$$\Omega_+(0, t) = r_1 \Omega_-(0, t) + t_1 \Omega_{inc}(t). \quad (4.36)$$

At the left mirror we have from 2.64

$$E_-(L, t) = r_2 E(L, t), \quad (4.37)$$

assuming no incoming field form the right side. Expressing the fields as

$$E_+(L, t) = \frac{\hbar}{2\mu_{ge}} \Omega_+(L, t) e^{-ik_L L} e^{i\omega_L t}, \quad (4.38)$$

$$E_-(L, t) = \frac{\hbar}{2\mu_{ge}} \Omega_-(L, t) e^{ik_L L} e^{i\omega_L t}, \quad (4.39)$$

result in

$$\Omega_-(L, t) = r_2 \Omega_+(L, t) e^{-i2k_L L}. \quad (4.40)$$

Here we have another example in which were we have an unwanted term, $e^{-i2k_L L}$, which we can't remove in a simple fashion. The term will therefore introduce a phase change to the reflected Rabi frequency, unless the exponent equals $2k_L L = 2\pi q$, for some integer q . This is the case when the laser frequency is matched to a cavity mode (assuming a cold cavity), such that

$$\omega_L = \frac{\pi c_0 q}{nL}, \quad q = 1, 2, 3, \dots \quad (4.41)$$

which is equivalent to the expression for the cavity mode in 2.72.

Complete equations

We conclude this section by summarizing the equations derived. The field is described by

$$\begin{pmatrix} -1 & 0 \\ 0 & 1 \end{pmatrix} \frac{\partial \Omega}{\partial z} - \frac{n}{c_0} \frac{\partial \Omega}{\partial t} = \frac{i}{2\pi} \int_{-\infty}^{\infty} \alpha(\delta) \{(\mathbf{u} + i\mathbf{v})\} d\delta, \quad (4.42)$$

with boundary conditions

$$\begin{aligned}\Omega_+(0, t) &= r_1\Omega_-(0, t) + t_1\Omega_{inc}(t), \\ \Omega_-(L, t) &= r_2\Omega_+(L, t)e^{-i2k_L L}.\end{aligned}\tag{4.43}$$

The Bloch equations were determined to be

$$\dot{\mathbf{R}} = \mathbf{A}\mathbf{R} + \boldsymbol{\varphi} + \boldsymbol{\xi},\tag{4.44}$$

with \mathbf{A} defined in 4.19.

4.2 Discretization

In this section we will discretize the equations in order to solve them numerically. The choice of numerical method is based loosely on numerical differential theory, however the motivation is basically that the chosen method were deemed have the best performance, in regard to speed, accuracy and stability when testing was performed.

The system is composed of two equation systems which runs simultaneously (they are calculated at the same time iteration), namely the Maxwell equation in 4.42 and the Bloch equations in 4.44.

The Maxwell equation can be regarded as an inhomogeneous advection equation [12], where the inhomogeneous part is dependant on the Bloch equations. The Bloch equations are more of a first order non-linear initial value problem. The tricky part lies in the fact that the system interact with each other, so for each step in time, one has to calculate the next iteration in both systems simultaneously.

We note that the grid is chosen equidistant in the space, time and frequency domain as

$$\begin{aligned}z_n &= (n - 1)\Delta z, & n &= 1, \dots, N_z, \\ t_i &= (i - 1)\Delta t, & i &= 1, \dots, N_t, \\ \delta_m &= \delta_{min} + (m - 1)\Delta\delta, & m &= 1, \dots, N_\delta,\end{aligned}$$

where

$$\begin{aligned}\Delta z &= \frac{L}{N_z - 1}, \\ \Delta t &= \frac{T}{N_t - 1}, \\ \Delta\delta &= \frac{\delta_{max} - \delta_{min}}{N_\delta - 1}.\end{aligned}$$

Here we have that L is the length of the cavity, N_z the number of grid points in space, T the duration of the simulation, N_t the number of grid points in time, δ_{max} the maximum detuning, δ_{min} the minimum detuning and N_δ the number of grid points in the detuning range.

The procedure is the following. The outer loop consist of iterating through the time grid. For each iteration t_i in time, we begin by calculating the next time step for the Bloch equations at time t_{i+1} , using an explicit method for each coordinate z_n in space and for each δ_m in detuning. The resulting Bloch vector at grid point $i + 1$ can then be used to calculate the electric field at time t_{i+1} at all z_n -points.

4.2.1 Bloch equation

The Bloch equations will be calculated simultaneously, but separately from the Maxwell equations for each iteration in time. The method used is called the *Adam Bashforth method* [7, 12], which is an explicit linear multistep method. We will use the four step variant, which reads

$$u_{i+1} = u_i + \frac{\Delta t}{24} (55f_i - 59f_{i-1} + 37f_{i-2} - 12f_{i-3}), \quad (4.45)$$

for differential equation

$$\frac{\partial u}{\partial t} = f(t, u). \quad (4.46)$$

Note that

$$f_i = f(t_i, u_i). \quad (4.47)$$

In our case we have a equation system looking like

$$\dot{\mathbf{R}} = \mathbf{A}\mathbf{R} + \boldsymbol{\varphi}. \quad (4.48)$$

Using the method above we get

$$\mathbf{R}_{i+1} = \mathbf{R}_i + \frac{\Delta t}{24} (55\mathbf{F}_i - 59\mathbf{F}_{i-1} + 37\mathbf{F}_{i-2} - 12\mathbf{F}_{i-3}), \quad (4.49)$$

where

$$\mathbf{F}_i = \mathbf{A}_i\mathbf{R}_i + \boldsymbol{\varphi}. \quad (4.50)$$

The matrix \mathbf{A}_i is calculated using 4.19 and updated with the new value of $\boldsymbol{\Omega}_i$ at each point i .

4.2.2 Maxwell equation

Quite a few methods were tested during the project, such as the *Crank-Nicolson-method*¹ [12], however we limit ourself in only presenting the method used in this thesis.

We will use a second order central difference approximation in space, while we in the time domain make the assumption that the time derivatives can be neglected.

The motivation for this assumption is the fact that we are only simulating very low frequencies, in this thesis for example we never go higher than 30 MHz in detuning (except in the beginning in section 3.4.1). This translates to a wavelength of roughly $\lambda = 5.5\text{m}$ (using $c_0/n = \lambda\nu$), which is several orders of magnitudes larger than the cavity length of roughly $L = 0.8\text{mm}$.

Usually it's required for this type of equation that the numerical grid has to be chosen so that

$$\frac{c_0\Delta t}{n\Delta z} \leq 1, \quad (4.51)$$

¹This method resulted in quite good output, however the computation times were simply too high for practicality.

due to stability reasons². If we for example only uses four grid points in space, so that $\Delta z = 0.2$ mm, we will receive a limit of the maximum time step as

$$\Delta t \leq \frac{n\Delta z}{c_0} = 1.2 \cdot 10^{-12} \text{ s}, \quad (4.52)$$

(using $n = 1.8$) which is a very small time step when the maximum frequency is only 30 MHz, so there is little change in the incoming field between several time steps. Condition 4.51 hence result in a oversized sample size in time, since we have such small values of L (Δz can't be chosen larger than L).

Thus we make the assumption that as long as the timesteps are relatively short compared to the maximum involved frequency, we can neglect the time derivative. In the result section, Δt was chosen so that the largest detuning frequency is resolved by at least 30 steps in time, which may result in some error at the edge of the spectrum, however is proven to provide good result in most of the spectrum. Choosing a lower amount steps in time than this however, result in instability.

We write the Maxwell equation in 4.42 as an equation system,

$$-\frac{\partial \Omega_+}{\partial z} - \frac{n}{c_0} \frac{\partial \Omega_+}{\partial t} = f_+, \quad (4.53)$$

$$\frac{\partial \Omega_-}{\partial z} - \frac{n}{c_0} \frac{\partial \Omega_-}{\partial t} = f_-, \quad (4.54)$$

where the inhomogeneous parts f_+ and f_- are

$$\mathbf{f} = \begin{pmatrix} f_+ \\ f_- \end{pmatrix} = \frac{i}{2\pi} \int_{-\infty}^{\infty} \alpha(\delta) \{(\mathbf{u} + i\mathbf{v})\} d\delta. \quad (4.55)$$

This term is easily calculated at each grid point $[i, n]$ as

$$\mathbf{f}_{i,n} = \frac{i\Delta\delta}{2\pi} \sum_{m=1}^{N_\delta} \alpha_m(\mathbf{u}_{i,n,m} + i\mathbf{v}_{i,n,m}). \quad (4.56)$$

Neglecting the derivatives then result in

$$-\frac{\partial \Omega_+}{\partial z} = f_+, \quad (4.57)$$

$$\frac{\partial \Omega_-}{\partial z} = f_-. \quad (4.58)$$

We now have a boundary value problem, which we recalculate for each time step, after having calculated the Bloch components $\mathbf{u}_{i,n,m}$ and $\mathbf{v}_{i,n,m}$ for the $\mathbf{f}_{i,n}$ -term.

As a final note, we only calculate the forward field at spatial grid interval $n = [2, N_z]$ and $n = [1, N_z - 1]$ for the backward field. The reason is that the forward field at $n = 1$ is defined by the boundary condition in equation 4.36, and the backward field at point $n = N_z$ by equation 4.40, so there is no need to include these points in the grid since they are already known and need no derivation is needed.

²In this case stability means that the involving fields don't grow out of bounds.

Spatial Derivatives

The spatial derivatives are determined using the central difference approximation, which is of second order accuracy,

$$\begin{aligned}\frac{\partial \Omega_+^{(i,n)}}{\partial z} &= \frac{\Omega_+^{(i,n+1)} - \Omega_+^{(i,n-1)}}{2\Delta z}, \\ \frac{\partial \Omega_-^{(i,n)}}{\partial z} &= \frac{\Omega_-^{(i,n+1)} - \Omega_-^{(i,n-1)}}{2\Delta z}.\end{aligned}$$

The boundaries require special attention. We look at the forward and backward field separately.

The forward field at $[i, N_z]$ must be differentiated differently, since the grid point at $[i, N_z + 1]$ doesn't exist. This is solved by an asymmetrical difference approximation [7],

$$\frac{\partial \Omega_+^{(i, N_z)}}{\partial z} = \frac{3\Omega_+^{(i, N_z)} - 4\Omega_+^{(i, N_z-1)} + \Omega_+^{(i, N_z-2)}}{2\Delta z}. \quad (4.59)$$

Since this approximation is of second order, we don't compromise the accuracy of the approximation as a whole.

At point $[i, 2]$ we simply use the boundary condition 4.36 at $[i, 1]$ and the central difference formula,

$$\frac{\partial \Omega_+^{(i, 2)}}{\partial z} = \frac{\Omega_+^{(i, 3)} - \Omega_+^{(i, 1)}}{2\Delta z} = \frac{\Omega_+^{(i, 3)} - r_1\Omega_-^{(1, i)} - t_1\Omega_{inc}^{(i)}}{2\Delta z}. \quad (4.60)$$

For the backward field we have to use the asymmetrical difference approximation at grid point $[i, 1]$,

$$\frac{\partial \Omega_-^{(i, 1)}}{\partial z} = \frac{-3\Omega_-^{(i, 1)} + 4\Omega_-^{(i, 2)} - \Omega_-^{(i, 3)}}{2\Delta z}. \quad (4.61)$$

At $[i, N_z - 1]$ we use the boundary conditions in 4.40 so that

$$\frac{\partial \Omega_-^{(i, N_z-1)}}{\partial z} = \frac{\Omega_-^{(i, N_z)} - \Omega_-^{(i, N_z-2)}}{2\Delta z} = \frac{r_2 e^{-i2k_L L} \Omega_+^{(N_z, i)} - \Omega_-^{(i, N_z-2)}}{2\Delta z}. \quad (4.62)$$

Reformulating into a matrix system

We now introduce the field vector which consist the electric field values at all points in the spatial grid, excluding the boundary condition points,

$$\mathbf{u}_+^{(i)} = \begin{pmatrix} \Omega_+^{(i, 2)} \\ \vdots \\ \Omega_+^{(i, N_z)} \end{pmatrix}, \quad (4.63)$$

$$\mathbf{u}_-^{(i)} = \begin{pmatrix} \Omega_-^{(i, 1)} \\ \vdots \\ \Omega_-^{(i, N_z-1)} \end{pmatrix}. \quad (4.64)$$

This formalism allows to express the spatial derivatives in matrix form as

$$\frac{\partial \mathbf{u}_+^{(i)}}{\partial z} = \mathbf{A}_+ \mathbf{u}_+^{(i)} + \mathbf{v}_+ \left(r_1 \Omega_-^{(1,i)} + t_1 \Omega_{inc}^{(i)} \right), \quad (4.65)$$

$$\frac{\partial \mathbf{u}_-^{(i)}}{\partial z} = \mathbf{A}_- \mathbf{u}_-^{(i)} + \mathbf{v}_- r_2 e^{-i2k_L L} \Omega_+^{(N_z,i)}, \quad (4.66)$$

where

$$\mathbf{A}_+ = \frac{1}{2\Delta z} \begin{pmatrix} 0 & 1 & 0 & 0 \\ -1 & 0 & 1 & \\ & \ddots & \ddots & \ddots \\ & & -1 & 0 & 1 \\ 0 & & 1 & -4 & 3 \end{pmatrix},$$

$$\mathbf{v}_+ = \frac{1}{2\Delta z} \begin{pmatrix} -1 \\ 0 \\ \vdots \end{pmatrix},$$

$$\mathbf{A}_- = \frac{1}{2\Delta z} \begin{pmatrix} -3 & 4 & -1 & 0 \\ -1 & 0 & 1 & \\ & \ddots & \ddots & \ddots \\ & & -1 & 0 & 1 \\ 0 & & 0 & -1 & 0 \end{pmatrix},$$

$$\mathbf{v}_- = \frac{1}{2\Delta z} \begin{pmatrix} \vdots \\ 0 \\ 1 \end{pmatrix}.$$

We can develop the system further by expressing $\Omega_-^{(1,i)}$ and $\Omega_+^{(N_z,i)}$ as,

$$\Omega_-^{(1,i)} = (1 \ 0 \ \dots) \mathbf{u}_-^{(i)},$$

$$\Omega_+^{(N_z,i)} = (\dots \ 0 \ 1) \mathbf{u}_+^{(i)},$$

thus we receive

$$r_1 \mathbf{v}_+ \Omega_-^{(1,i)} = \mathbf{N}_- \mathbf{u}_-^{(i)},$$

$$r_2 e^{-i2k_L L} \mathbf{v}_- \Omega_+^{(N_z,i)} = \mathbf{N}_+ \mathbf{u}_+^{(i)},$$

where

$$\mathbf{N}_- = \frac{r_1}{2\Delta z} \begin{pmatrix} -1 & 0 & \dots \\ 0 & 0 & \\ \vdots & & \ddots \end{pmatrix}, \quad (4.67)$$

$$\mathbf{N}_+ = \frac{r_2 e^{-i2k_L L}}{2\Delta z} \begin{pmatrix} \ddots & 0 & \vdots \\ 0 & 0 & \\ \dots & & 1 \end{pmatrix}. \quad (4.68)$$

Our derivatives are then

$$\frac{\partial \mathbf{u}_+^{(i)}}{\partial z} = \mathbf{A}_+ \mathbf{u}_+^{(i)} + \mathbf{N}_- \mathbf{u}_-^{(i)} + \mathbf{v}_+ t_1 \Omega_{inc}^{(i)}, \quad (4.69)$$

$$\frac{\partial \mathbf{u}_-^{(i)}}{\partial z} = \mathbf{A}_- \mathbf{u}_-^{(i)} + \mathbf{N}_+ \mathbf{u}_+^{(i)}. \quad (4.70)$$

We are now ready to fully express our method. Expanding 4.58 into matrix form and inserting our derivatives result in

$$\mathbf{A}_+ \mathbf{u}_+^{(i)} + \mathbf{N}_- \mathbf{u}_-^{(i)} = -\mathbf{f}_+^{(i)} - \mathbf{v}_+ t_1 \Omega_{inc}^{(i)}, \quad (4.71)$$

$$\mathbf{A}_- \mathbf{u}_-^{(i)} + \mathbf{N}_+ \mathbf{u}_+^{(i)} = \mathbf{f}_-^{(i)}, \quad (4.72)$$

where

$$\mathbf{f}_+^{(i)} = \begin{pmatrix} f_+^{(i,2)} \\ \vdots \\ f_+^{(i,N_z)} \end{pmatrix}, \quad (4.73)$$

$$\mathbf{f}_-^{(i)} = \begin{pmatrix} f_-^{(i,1)} \\ \vdots \\ f_-^{(i,N_z-1)} \end{pmatrix}. \quad (4.74)$$

The final step is now to mesh these two equation together, forming

$$\mathbf{X} \mathbf{u}^{(i)} = \mathbf{M}^{(i)}, \quad (4.75)$$

where

$$\mathbf{u}^{(i)} = \begin{pmatrix} \mathbf{u}_+^{(i)} \\ \mathbf{u}_-^{(i)} \end{pmatrix}, \quad (4.76)$$

$$\mathbf{X} = \begin{pmatrix} \mathbf{A}_+ & \mathbf{N}_- \\ \mathbf{N}_+ & \mathbf{A}_- \end{pmatrix}, \quad (4.77)$$

$$\mathbf{M}^{(i)} = \begin{pmatrix} -\mathbf{f}_+^{(i)} + \mathbf{v}_+ t_1 \Omega_{inc}^{(i)} \\ \mathbf{f}_-^{(i)} \end{pmatrix}. \quad (4.78)$$

Solving the system

The final step is to solve equation 4.75, in terms of $\mathbf{u}^{(i)}$, for every timestep t_i to t_{i+1} . One could obviously do this by calculating the inverse of \mathbf{X} , however this is usually a cumbersome way to solve a problem in a numerical environment, especially when we have to solve the same system over again for different input vectors $\mathbf{M}^{(i)}$.

Usually one resorts to some form of matrix factorization method, for example using LU decomposition [11, 6]. The advantage is that the resulting system generally requires a lower amount of additions and multiplications to solve, hence reduced computing time. The factorization can also be stored for multiple uses.

We will not go into detail about this subject here, since the matrix system in our case will be relatively small, however we mention that we will use an

user developed MATLAB kit [6] for the factorization. Normally one can use the MATLAB included backslash operation, shown below is an example for solving $Ax = y$.

```
x = A\y;
```

This method has a set of decomposition methods to select from in order to solve the problem, and can be considered to quite powerful. A drawback however is that the factorization performed can't be reused, hence if we have multiple systems with the same matrix A , we will needlessly perform the same decomposition repeatedly.

The kit cited above provides an object oriented function, called *factorize*, with output being an object which contains the factorization of the input matrix. The factorization object can then be used multiple times. An example of MATLAB code for solving several systems $Ax_i = y_i$ looks like

```
U = factorize(A);
for i = 1:N
x(:,i) = U\y(:,i);
end
```

4.3 Result

We now present some result from the new simulator.

The grid is chosen with $N_z = 15$ steps in space, $N_\delta = 3000$ in detuning and $N_t = 37700$ in time. The time duration of the simulation is approximately $50 \mu\text{s}$, with a computation time of roughly 30 min.

We also note that the Γ coefficient is chosen small, around $1/360$. Otherwise are parameters such as reflection reflection coefficients chosen the same, being $R_1 = 0.8$ and $R_2 = 0.997$.

4.3.1 A note on the input field used

The input or incoming field will be defined as in 4.9, so the question is how to choose parameters $\xi(z, t)$ and $\varphi(t)$. ξ determines the overall shape or envelope of the pulse, while $\varphi(t)$ is the phase which varies time.

The chosen pulse shape will be the Supergaussian function, which is a more general version of the Gaussian shape, however it uses an higher order of power over the exponent (the power of an Gaussian is two). The function is

$$\xi(t) = \xi_0 \exp \left[-\frac{1}{2} \left(\frac{t - t_0}{\sigma} \right)^P \right], \quad (4.79)$$

$$\sigma = \frac{t_{FWHM}}{2 \sqrt[2]{2 \log(2)}}, \quad (4.80)$$

where t_{FWHM} is the full half width maximum of the envelope, t_0 the center of the pulse and P the power. Choosing $P = 10$ result in square like pulse with rounded edges.

Concerning $\varphi(t)$, we note that we are interested in a readout pulse with large spectral width which at least covers the absorption profile. This is achieved by choosing $\varphi(t)$ as

$$\varphi(t) = \varphi_0 t + \frac{1}{2} \varphi_k t^2, \quad (4.81)$$

where φ_0 and φ_k are constants. The detuning δ frequency of the pulse is then linearly time dependant [19] as

$$\delta(t) = \frac{\partial \varphi}{\partial t} = \varphi_0 + \varphi_k t \quad (4.82)$$

A typical readout pulse used in the simulations is presented in figure 4.1. As seen in the spectral density graph, we receive the desired broad spectral width. In all simulations performed the pulse is chosen so that it covers most of the chosen absorption spectrum.

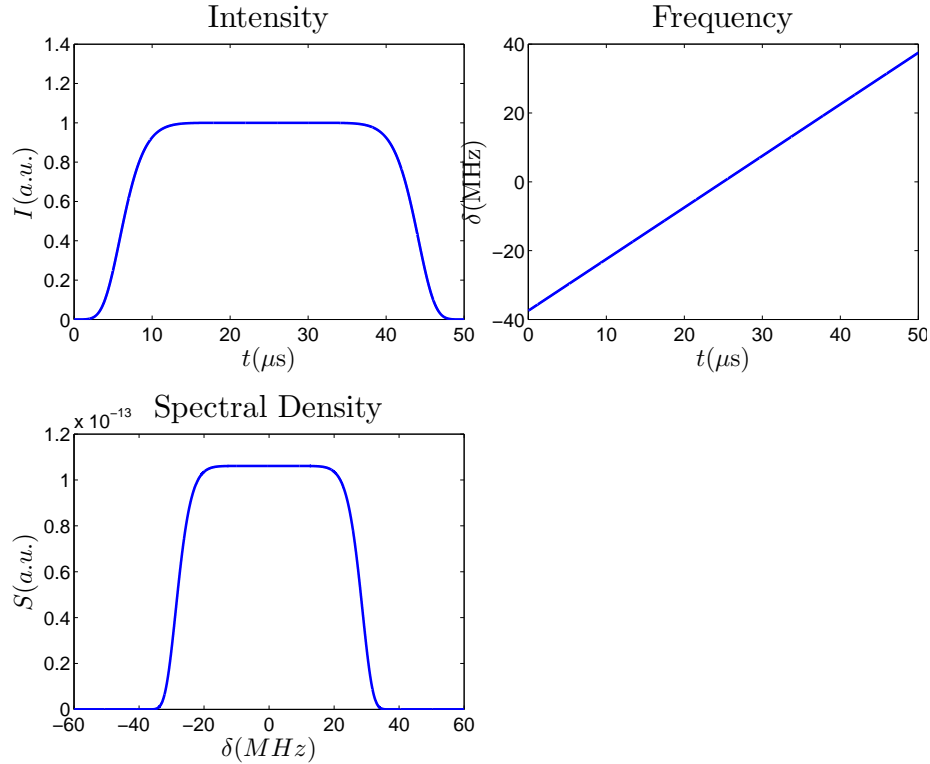


Figure 4.1: Upper left graph shows the intensity as a function of time, the upper right graph the frequency as a function of time and the lower left the spectral density or intensity (this is calculated by applying the fourier transform on the field).

4.3.2 Relative error

We are interested in comparing the original and computed absorption spectrum for each simulated data set, hence we define an error function which will be used

below.

Assuming a data set of $\alpha_{\mathbf{0}}(\omega)$ (the original absorption spectrum) and $\alpha_{\mathbf{c}}(\omega)$ (the computed absorption spectrum), we define the relative error as

$$\text{err}(\omega) = \left| \frac{\alpha_{\mathbf{0}}(\omega) - \alpha_{\mathbf{c}}(\omega)}{\max[\alpha_{\mathbf{0}}(\omega)]} \right|. \quad (4.83)$$

4.3.3 Some different cases

As in the previous chapter, we will look at four cases, with different cavity lengths for each. The lengths are chosen the same as those in the previous chapter, as shown in table 4.1. The absorption spectrum is also identical in these cases.

Table 4.1: Cavity lengths for each investigated case.

Case	L
1	0.7999942 mm
2	0.7999622 mm
3	0.7999462 mm
4	0.8000262 mm

We begin by showing how the electric fields looks in the time domain. In figure 4.2 we see the incoming, reflected and transmitted fields, when the length of case 3 is used. Most of the transmission occur in the centre of the pulse, which is expected since this is the region where frequency of the pulse matches the AFC structure.

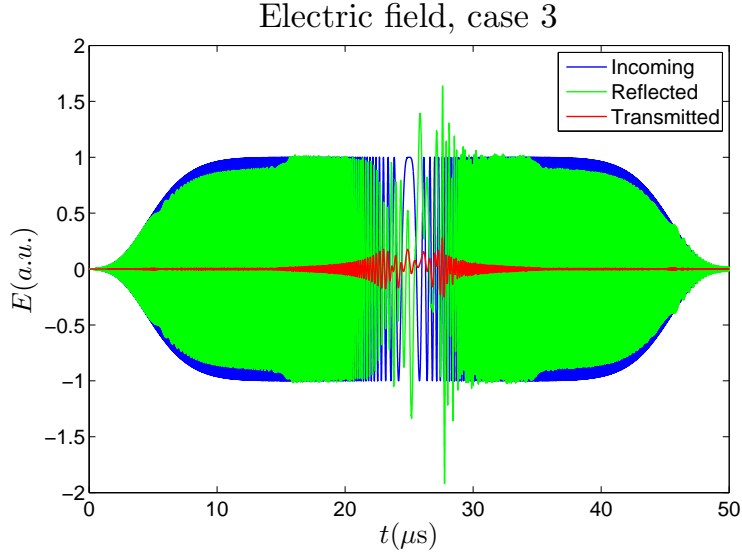


Figure 4.2: The incoming, reflected and transmitted fields, resulting from a simulation with an absorption spectrum as shown in 4.10.

In figure 4.3, 4.5, 4.9 and 4.11 we plot the transmission and reflection spectra, for each of the four cases. For each figure we look at both the case of an empty well and the case with AFC peaks included. In figure 4.4, 4.6, 4.10 and 4.12 we show the original and computed absorption spectrum for each case in the same order, with an error plot using formula 4.83 included as well. For comparison we refer to the older simulations in the previous figures 3.6 to 3.9 in the AT-chapter, where we used Axel's interference simulator.

Note that only method 2 of the analysing algorithm is used in this section, since both methods provide near identical result anyway, as was the case in the result section in the AT-chapter.

We begin with noting the similarity when comparing to the spectra in the AT-chapter, and we see that the error as shown in the error plots in most of the cases are around a few percent. Overall the discrepancy is low.

However a deviation occurs in the case 2 in figure 4.5 and 4.6. In the reflection spectrum we can observe some noise in the centre region, which result in some quite high peaks of almost 9% in the error plot. This feature is strikingly similar to what was seen in the output from the MB-simulations in Axel Thuressons thesis [21], where this phenomena was attributed to an optical beating effect between the light and dipoles.

While this could be the case here as well, it is more likely that this is some numerical artefacts. In 4.5 the reflection and transmission from a simulation with a larger set of detuning points, being $N_\delta = 5000$ in this case (other parameters are the same as in case 2). The absorption and error is plotted in figure 4.8 as well. The error is reduced significantly, so it's reasonable to assume that the simulator for larger sample sizes will converge to a solution in which these artefacts disappear.

The problem is likely due to the term $e^{-i2k_L L}$ in equation 4.40, which describes the boundary condition at mirror 2. In case 3 we have matched the cavity mode to the centre laser frequency ω_L , so this term is equal to 1 in this case ($2k_L L = 2\pi$), which is why this discrepancy doesn't appear here.

This indicates that the code could be made more robust. However as seen in the other cases, we get a fairly good match between the expected and calculated absorption, so the result still have some value.

4.3.4 Noise sensitivity

In real experiments there will always be some sort of pollution in the measurement samples, due various outside perturbations such as background noise and shot noise. Hence it's of interest to investigate in what degree our analysing tool still can operate when we have imperfect data. The analysis will be done for both method 1 and 2, in order to see if there is any advantage for any of them. We use the data from case 3, shown in figure 4.9 for our noise sensitivity test, which is the case when we have matched the cavity mode with the centre of well.

The test is performed by applying a white noise signal to all included fields, being the incoming, reflected and transmitted field. The Signal to Noise Ratio (SNR) is defined relative to the incoming field. We also reduce the sample size of the fields, since this also is a limit during an experiment. Sample size is reduced to $N_t = 10000$.

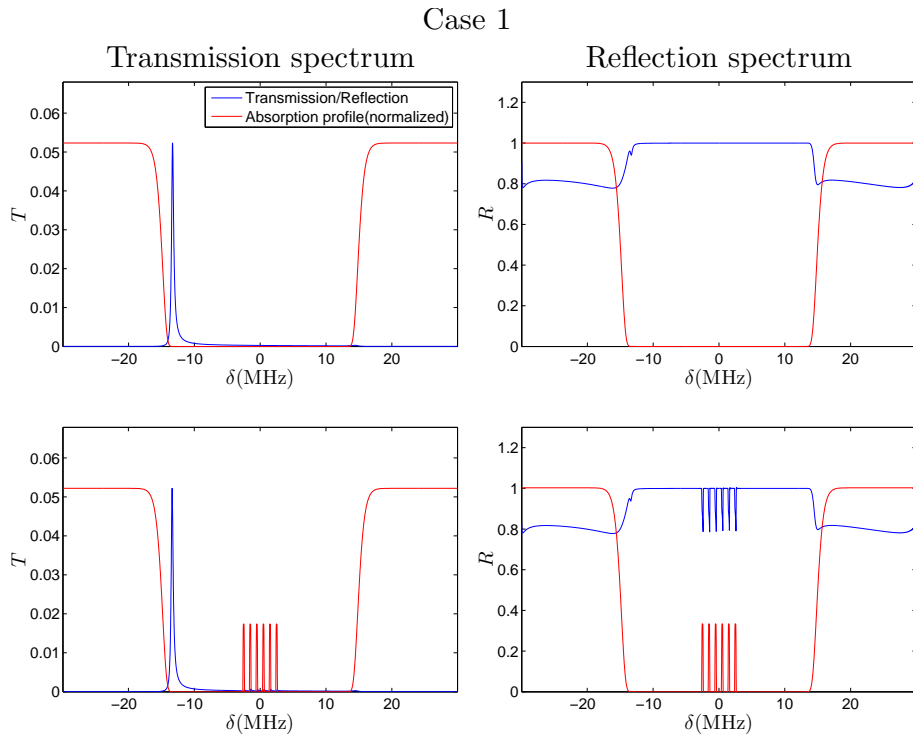


Figure 4.3: Transmission and reflection lines versus absorption profile. In the upper two graphs we have excluded the AFC peaks, while they have been included in the lower graphs. The mode is positioned at the edge of the well.

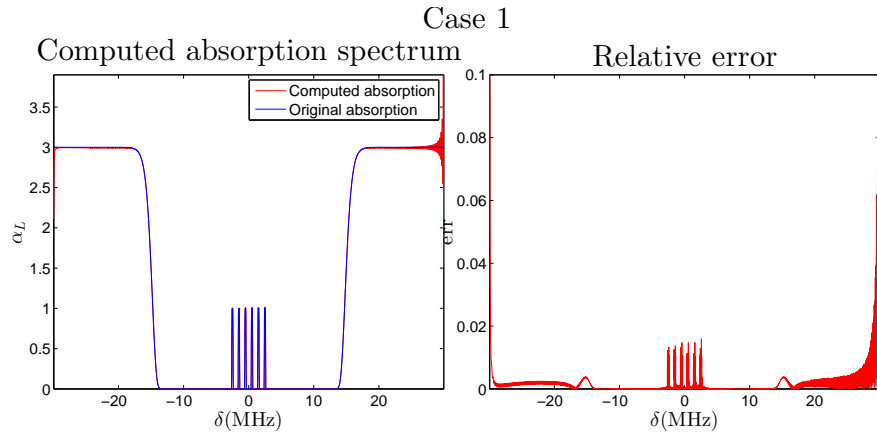


Figure 4.4: Calculated and original absorption spectrum is shown to the left, while a relative error plot is shown the right.

In figure 4.13 we have used method 1 to compute the absorption, for three

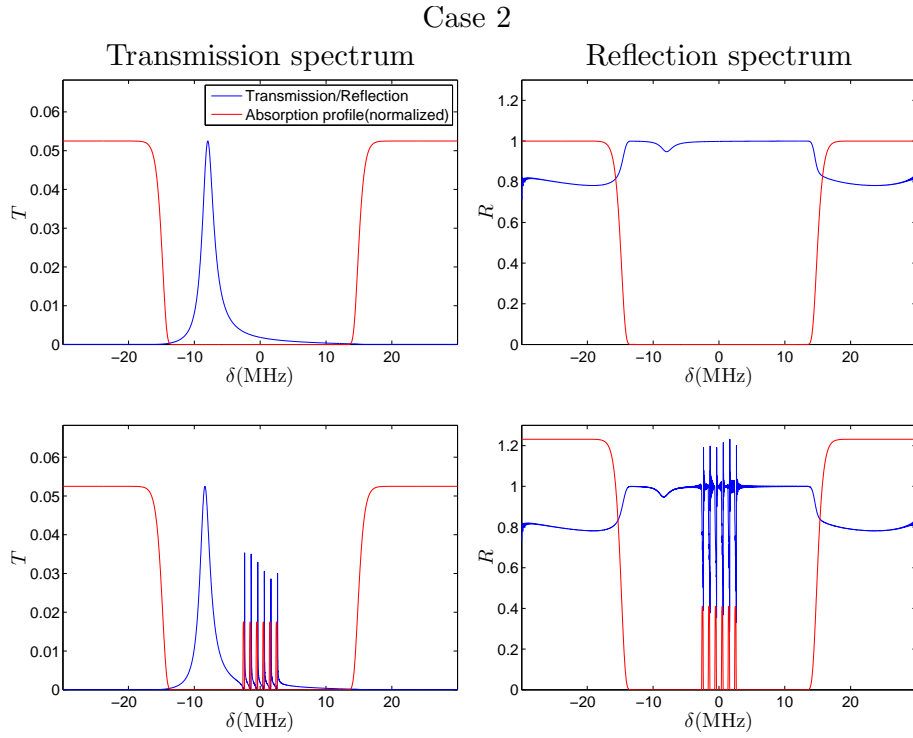


Figure 4.5: Transmission and reflection lines versus absorption profile. In the upper two graphs we have excluded the AFC peaks, while they have been included in the lower graphs. The mode is positioned between the edge and center of the well.

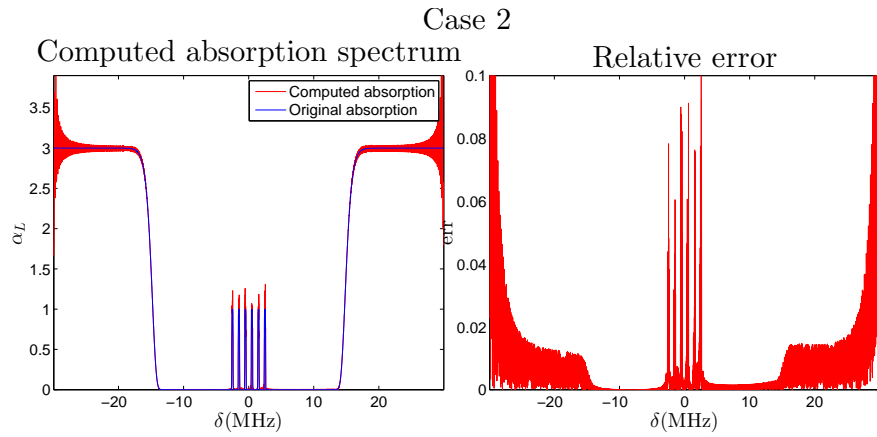


Figure 4.6: Calculated and original absorption spectrum is shown to the left, while a relative error plot is shown the right.

different levels of noise. The transmitted field envelope³. is shown as well, so

³The envelope of a field $E(t)$ is here defined as $|E(t)|$, which in this case is a visually more

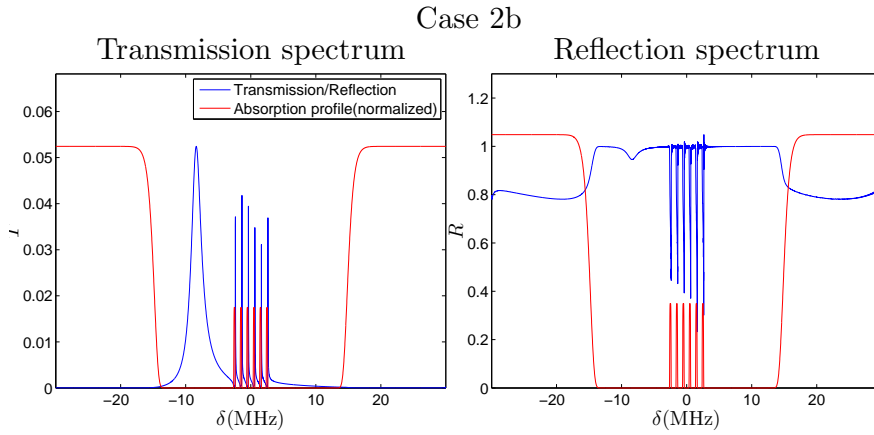


Figure 4.7: Transmission and reflection lines versus absorption profile, with same parameters as in previous figure with case 2, however with an increased number of grid points in detuning ($N_\delta = 5000$).

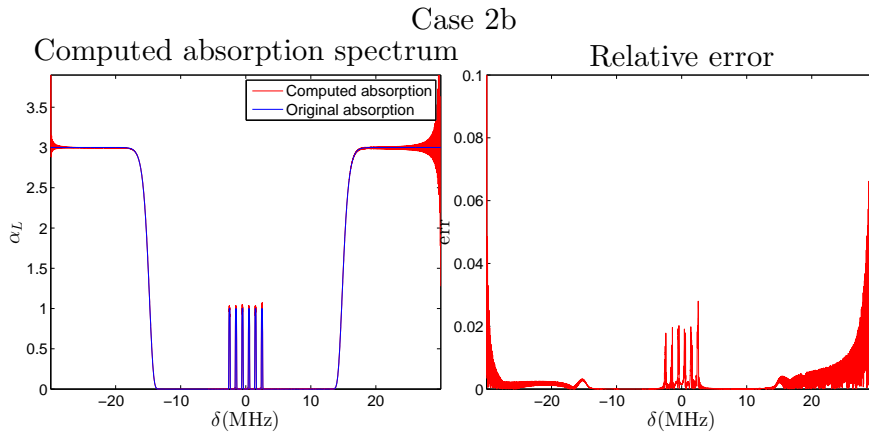


Figure 4.8: Calculated and original absorption spectrum is shown to the left, while a relative error plot is shown the right. The parameters are the same as in case 2, however with an increased grid size of $N_\delta = 5000$.

that we can get a sense of how noisy the signal actually is. In 4.14 the relative error is shown between the original and computed profile, for different SNR. As a reminder, method 1 uses all fields for its calculation.

It's very clear that noise reduces the performance by a high degree, though it seems that the error mostly affect the edges of the spectrum. In the middle we gain still get a good sense of the structure of the peaks. In the case of an SNR of 50, we get an maximum error of 14% when looking at the AFC peaks region, which at least gives us an good sense of the structure, though it's not enough for measurement purposes.

available than the appearance in figure 4.2

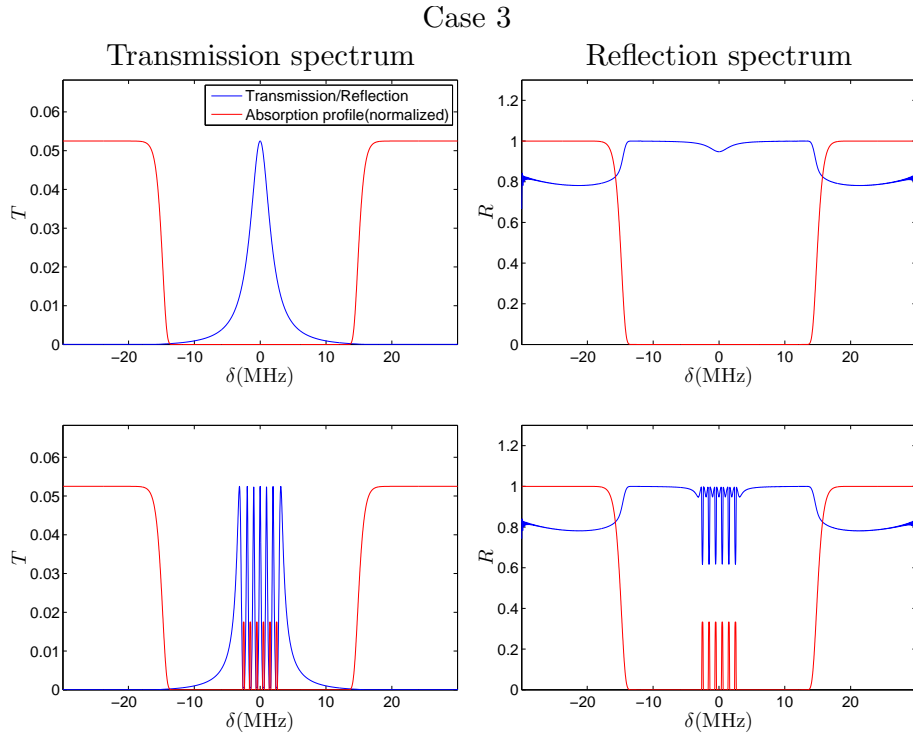


Figure 4.9: Transmission and reflection lines versus absorption profile. In the upper two graphs we have excluded the AFC peaks, while they have been included in the lower graphs. The mode is positioned at the centre of the well.

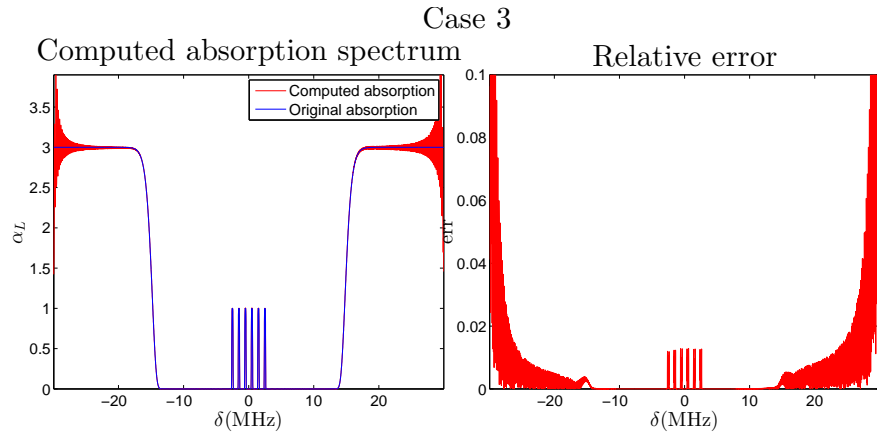


Figure 4.10: Calculated and original absorption spectrum is shown to the left, while a relative error plot is shown the right.

Next we perform the same test however now we make use of algorithm 2, which only need the incoming and reflected field for its computation. The absorption spectra are shown in figure 4.15 in the same manner, with reflected

Case 4

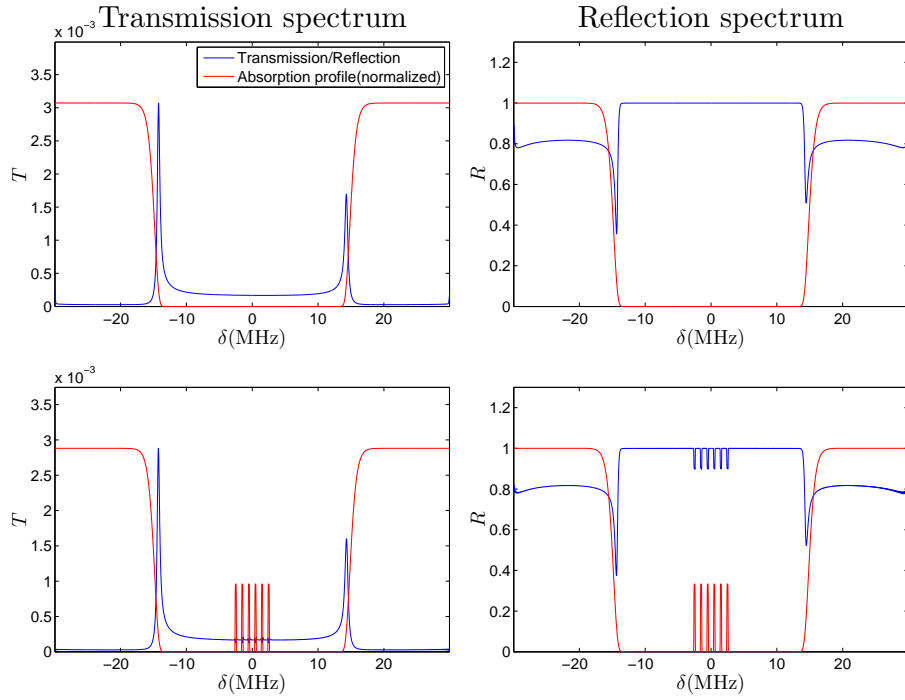


Figure 4.11: Transmission and reflection lines versus absorption profile. In the upper two graphs we have excluded the AFC peaks, while they have been included in the lower graphs. The mode appears to have been splitted into two modes.

Case 4

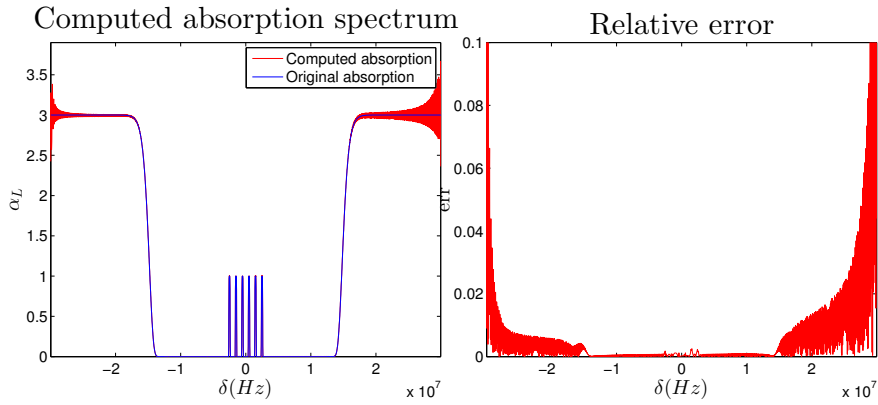


Figure 4.12: Calculated and original absorption spectrum is shown to the left, while a relative error plot is shown the right.

fields included instead. The error is shown in figure 4.16.

Method 2 clearly performs better than method 1, even the worst case for

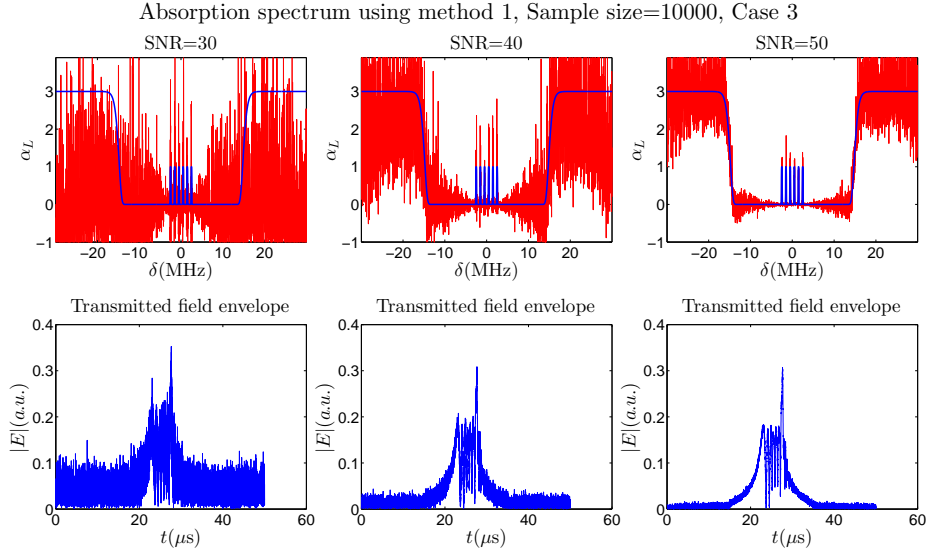


Figure 4.13: Calculated absorption spectrum, with noise applied over the input and output fields, as shown in the upper row for different SNR. Note that the SNR is relative to the input field. In the lower row are the transmitted field envelopes, with noise applied.

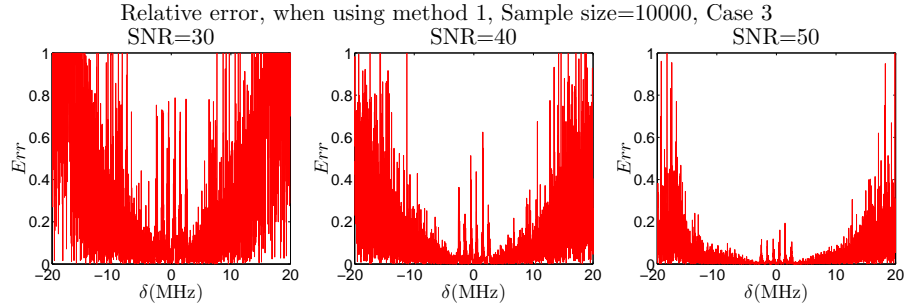


Figure 4.14: Relative error between the original and computed absorption spectrum, for different SNR.

method 2 is comparable with best case of method 1. However there is still a large amount of noise at the sides of the well, which is unfortunate but not of a major concern, since it's the AFC peaks which are ultimately the important component concerning qubit storage. In the error plot we see that the error is lower than around 4% and 2% in the comb region, in case of on SNR of 40 and 50 respectively. This can be considered acceptable in an experiment.

We conclude by including one final test. We perform the same test as above with algorithm 2, however we use the data from case 1 instead, shown in figure 4.3, which is the case where the cavity mode is positioned at the edge of the well. The noise plots are shown in figure 4.17 with error plots in figure 4.18. We can observe that the region with the lowest noise has been moved to the edge of the well, at roughly the same position as the cavity mode in figure 4.3.

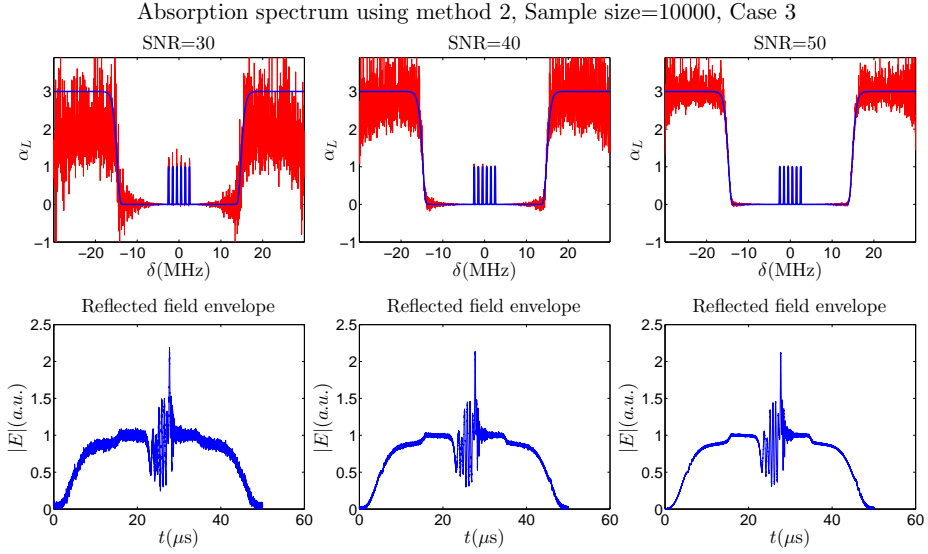


Figure 4.15: Calculated absorption spectrum using method 2, with noise applied over the input and output fields, as shown in the upper row for different SNR. In the lower row are the reflected field envelopes, with noise applied.

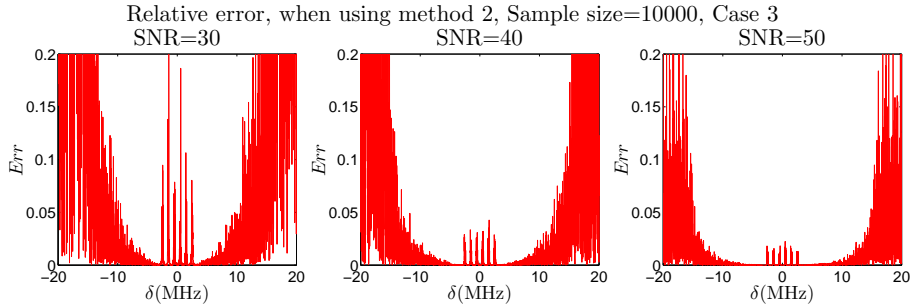


Figure 4.16: Relative error between the original and computed absorption spectrum, for different SNR.

4.4 Discussion

In this chapter we saw that the MB simulator performed adequately, in the sense that the discrepancy between the computed and original absorption spectrum were shown to be low, in the order of a few percents for most cases. This raises the hope that the analysing algorithm actually models the light-matter interaction to a sufficient degree for practical use.

We did see however that the simulator performs worse when the cavity structure doesn't match the laser frequency, though it seems like the output converges to the right solution for an increased grid size.

When noise was added over our signals, we saw that method 2 performs in a manner that can be considered sufficient, while method 1 was shown to perform poorly. The explanation for this lies in the fact that the transmitted fields will

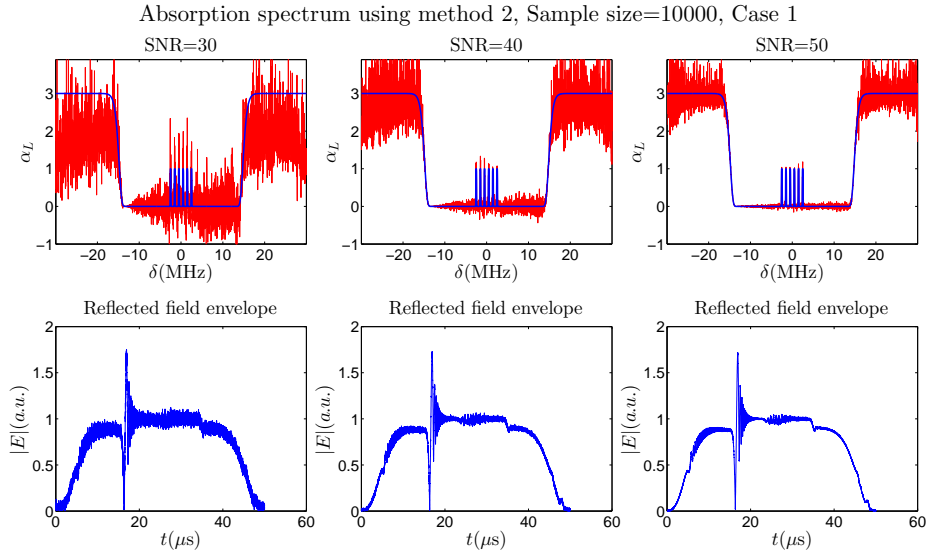


Figure 4.17: Calculated absorption spectrum, with noise applied over the input and output fields, as shown in the upper row for different SNR. In the lower row are the reflected field envelopes, with noise applied.

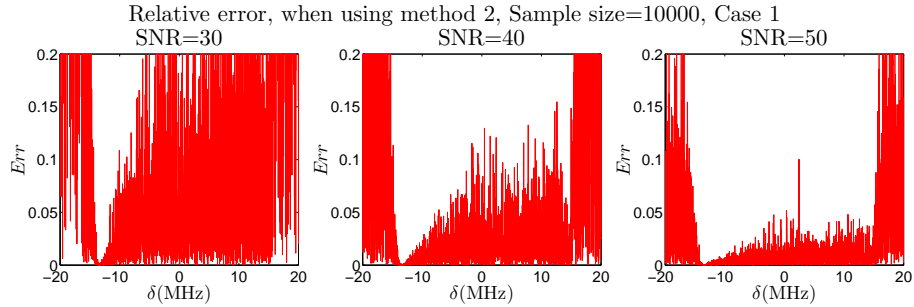


Figure 4.18: Relative error between the original and computed absorption spectrum, for different SNR.

generally be some order of magnitude lower than the incoming and reflected field, so the SNR will be quite bad in this case.

The reflected signal however is usually as strong as the incoming signal, so the SNR will be relatively good. This is quite apparent when comparing the transmitted signal in figure 4.13 and the clearer reflected signal in figure 4.15. Since method 2 only requires the reflected and incoming field, it isn't as affected by the noise as method 1. As a side-note it's also easier to construct an experimental setup which only require the measurement of two fields, so the fact that method 2 perform well is promising.

Lastly we also saw that it is preferable to place the cavity mode at the centre, since this reduces the noise in this region of the spectrum, however as long as the SNR is kept low, it doesn't affect the AT result to much.

Chapter 5

Experiment

The author of this report is not directly involved in the experimental phase of this project, which is still ongoing. However it's still in order to discuss how the algorithm can be applied in an experimental setup. We note that it's method 2 which will be used, due to the fact that it's both easier to implement in a experimental setup and performs better, as mentioned in the discussion in previous chapter.

The major hindrance when applying the analysing tool is the fact that the phase development of the incoming and reflected field are required. The detectors used however can only directly measure the intensity of the field, as a function of time, hence the phase is lost.

This problem can be solved using a reference wave for comparison. Two waves with different frequencies will interfere with each other in such a way that the total intensity is modulated over time¹. If we assume that we fully know the field of the reference wave, we should after an intensity measurement be able to compute the field of the other wave as well.

As a conceptual example, consider a reference wave and an unknown wave at the measuring coordinate, described by

$$E_{ref}(t) = E_0 \cos(\omega t), \quad (5.1)$$

$$E_2(t) = E'_0 \cos(\omega' t). \quad (5.2)$$

Parameters ω and E_0 is assumed to be fully known. The total intensity which we assume to be measurable, is then

$$\begin{aligned} I(t) &= |E_{ref}(t) + E_2(t)|^2 \\ &= |E_0|^2 + |E'_0|^2 + [E_0 E_0^* + E_0^* E'_0] \{ \cos[(\omega - \omega')t] + \cos[(\omega + \omega')t] \}, \end{aligned} \quad (5.3)$$

The expression consist of a constant and two oscillating parts with frequencies $\omega - \omega'$ (this is the part we can detect) and $\omega + \omega'$ (oscillates to rapidly for measurement). Since we have knowledge of ω , it's possible to determine the unknown ω' .

As seen in previous chapters, the electric field expression is usually a bit more complicated, however this example still serve as an idea on how the measurement can be performed.

¹This phenomena is called optical beating.

The best source for an reference should usually be the same as the laser source sent to the OQM, since the two interfering waves will be well correlated. It's required that the reference wave is modulated with some frequency shift, otherwise the frequency $\omega - \omega'$ part in 5.3 disappears or becomes too small for measurement.

The frequency shift can be achieved using using an Acousto Optic Modulator (AOM) [19], which make use of light-sound interaction in some medium, to alter the frequency of the light. In figure 5.1 an conceptual setup² is demonstrated.

In the setup, a semitransparent beam splitter is used to split up the laser light E_L into two beams. One of the beams is sent to the cavity, while the other is sent through an AOM (where it is frequency shifted with shift $\Delta\omega$) to the detector where it can be used as an reference wave. From the cavity crystal we receive an reflected beam with some unknown frequency ω' , which is sent towards the detector.

The detector does as a result measure the intensity interference from both the reflected light, and the frequency shifted reference light. We can then apply the argument above to calculate the phase of the reflected light, which should then allow us to apply method 2 to compute the absorption spectrum inside the cavity.

²A real experimental setup is of course more complex. Any technical details such as what laser is used or how the light polarization is modulated, is excluded.

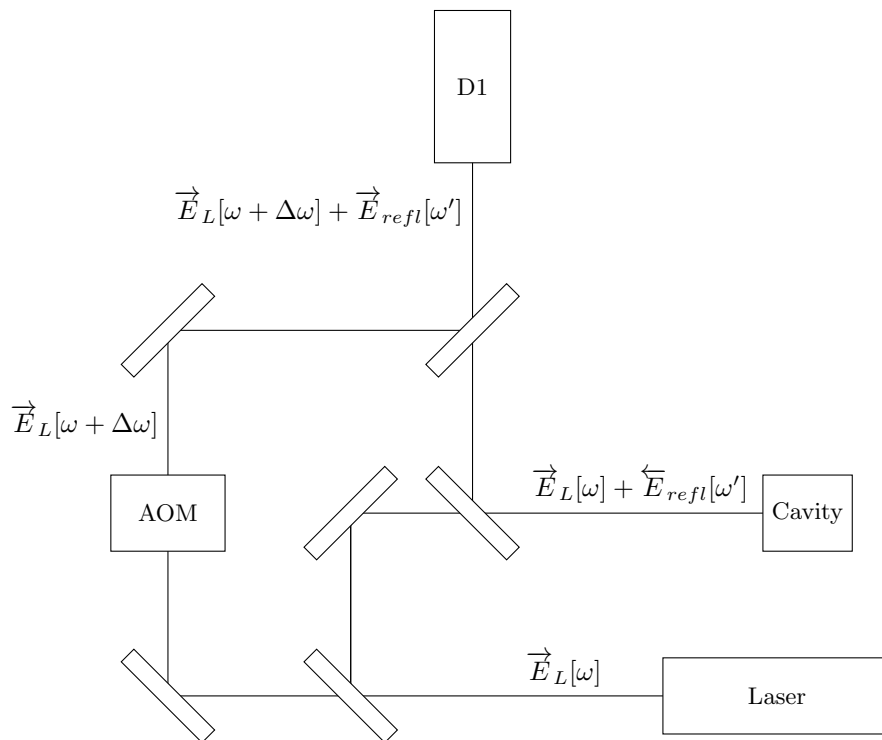


Figure 5.1: Illustration of an conceptual optical setup. Components consist of a laser source, an AOM, a set of mirrors (semitransparent or fully reflective), a detector denoted D1 and the cavity crystal.

Chapter 6

Summary

In this thesis an algorithm for analysing the absorption spectrum inside a cavity was developed. The validity and performance of the Analysing Tool (AT) was investigated using theoretical simulations based on the Bloch-Maxwell equations. Some of the simulations were developed by a previous master's thesis, however a new simulator was developed which was more suited to this thesis specific needs.

The AT can shortly be described to use the amplitude and phase of the input and output field from the cavity, to calculate the fields inside the cavity. Using a dispersion model, it compares the different calculated fields to see how much attenuation is introduced as a function of frequency, when a field propagates through the medium.

Two variants were presented, which differ in the formula used in the last step. The first variant requires all three fields (incoming, reflected and transmitted), while the second only needs the incoming and reflected light.

Both variants of the AT were concluded to work well in the simulated cases investigated. Method 2 was deemed to be the most suited, since it is less sensitive to noise in the signals than method 1. Also it's considerably easier to only measure two light sources instead of three as in the case of method 1 (assuming that we need to know phases of the fields, which is a requirement for the AT).

Further work that needs to be done is of course to apply the algorithm on some experimental measurement data, which unfortunately is not yet available, since the requirement of a phase profile of the waves is not trivial to fulfil and has not been done in this area of research as of yet.

Appendix A

Code

For documentation purposes, some general description of the MatLab code used in this thesis is presented here.

A.1 Simulator

The field outputs which were presented in the Maxwell-Bloch chapter, were calculated by

- *CalcCavityField*.

The function needs input such as cavity and material parameters, and some input field, defined as a function. There is also the option to show the progression of the cavity fields during the simulation, however this will reduce the computation speed.

Most subroutines are defined in the same script, however there are some functions defined separately used which can be found in the *Library* folder.

To run a simulation it's advised to use a main script which defines all parameters, grid and fields. For this one can use the template scripts

- *SimulationMainScript*. Defines all necessary parameters for *CalcCavityField*.
- *SetRun*. Used to initiate several simulations with different parameters. Basically it just changes some parameters for each run and calls *SimulationMainScript*. The output data is stored in a file for later use.

A.2 Library

Below is a list of general purpose functions used either for the simulator or visualisation purposes. All these functions are found in the *Library*-folder.

- *AtomicDistrubtion*. Defines a distribution which consist of a well with a set of AFC peaks (the same structure in all simulations conducted in this report).
- *Filter_SuperGauss* Applies a Supergaussian shaped filter in the frequency domain, over a time dependant data set.

- *FindIndex*. Finds the index i of a value in vector x , which is as close as possible to the predefined value of x_i .
- *findAlpha_1*. Calculates the absorption spectrum using algorithm 1, hence it requires the incoming, reflected and transmitted field from the cavity.
- *findAlpha_2*. Calculates the absorption spectrum using algorithm 2, hence it requires only the incoming and reflected field from the cavity.
- *Fourier*. Calculates the Fourier transform, with zero detuning in the middle of the spectrum.
- *FuncMatch*. Matches two data sets so that their grid points are the same. Extrapolation is used to match the functions at the shared grid points, so no information is neither destroyed or created. The purpose is to allow an easy comparison between data sets with different grids.
- *InstantFreq*. Calculates the instantaneous frequency for an input function, as a function of time. Useful to make sure that an pulse has the correct frequency development in time.
- *InvFourier*. Calculates the inverse Fourier transform, assuming the zero detuning point is in the middle of the spectrum.
- *ReadoutPulse*. Creates an frequency chirped pulse function with input parameters. One can choose from square, triangular, Supergaussian or Gaussian-shaped pulses.
- *Resize*. Reduces the sample size of a data set, which is often advisable to use before plotting. If a sample is very large it will take a long time to plot and will also result in a very sluggish graph to navigate in.
- *subaxis*. Provides an alternative to the *subplot* function, which allows easier editing of subplots. The code is third party developed¹.
- *truncate*. Truncates a data set to a certain grid interval. Useful when the grid interval needs to be reduced for a plot.

The following list are subroutines which is used in the simulation file *Calc-CavityField*

- *Node*. Is an object, which is used to store the Bloch vector values of detuning, for a specific coordinate in space and time.
- *PropagationMatrices*. Creates the matrices \mathbf{A} and \mathbf{v} , derived in the discretization part in Maxwell-Bloch simulator chapter.

There is also a file with stored universal constants for easy access, named *UniversalConstants*.

¹<http://www.mathworks.com/matlabcentral/fileexchange/3696-subaxis-subplot>

A.3 Visualization

There are some scripts which were used to visualize the data.

- *Reverse*. This script used the variables in the current workspace, and applies the Analysing Tool (AT) on the data (for this we use either *findAlpha_1* or *findAlpha_2*). Plots include transmission and reflection spectra, both original and computed absorption spectra and with an error-plot of the absorption as well.
- *PlotRun*. Loads a predefined set of files for the simulation data, and plots a similar set of plots like *Reverse*, for each file. This function was used to plot the different cases in the Maxwell-Bloch chapter.
- *testReverseToolNoiseFilter*. Similar to *Reverse*, however this script applies noise and filtering to the data, in order to test the sensitivity of the AT. Can also reduce the sample size. Was used to plot the the results in the Maxwell-Bloch chapter, where noise was applied.

Bibliography

- [1] M.Sabooni M.Huang S. Kröll M.Afzelius I.Usmani A. Amari, A.Walther and H. deRiedmatten N.Gisin B.Lauritzen, N. Sangouard. *Towards an efficient atomic frequency comb quantum memory. Journal of Luminescence*, 130, February 2010.
- [2] Mikael Afzelius and Christoph Simon. *Impedance-matched cavity quantum memory. Phys. Rev. A* 82, August 2010.
- [3] Barry C. Sanders Alexander I. Lvovsky and Wolfgang Tittel. *Optical quantum memory. Nature Photonics*, 231, November 2009.
- [4] L. Allen and J. H. Eberly. *Optical resonance and two-level atoms*. Dover publications, inc, New York, 1987.
- [5] Michael A.Nielsen and Isaac L.Chuang. *Quantum computation and quantum information*. Cambridge University Press, Cambridge, 2000.
- [6] Timothy A. Davis. *Algorithm 9xx, FACTORIZE: an object-oriented linear system solver for MATLAB*. Technical report, University of Florida, Unknown.
- [7] Lennart Edsberg. *Introduction to computation and modeling for differential equations*. John Wiley & Sons, Inc., New Jersey, 2008.
- [8] Christopher J. Foot. *Atomic physics*. Oxford University Press, Oxford, 2005.
- [9] Kazuyuki FUJII. *Introduction to the Rotating Wave Approximation (RWA) : Two Coherent Oscillations*. Yokohama City University, 2013.
- [10] J. I. Cirac H.-J. Briegel, W. Dür and P. Zoller. *Quantum Repeaters: The Role of Imperfect Local Operations in Quantum Communication. PHYSICAL REVIEW LETTERS*, VOLUME 81, December 1998.
- [11] A. Holst and V. Ufnarovski. *Matrix Theory*. LTH, Lund, 2011.
- [12] Arieh Iserles. *A first course in the numerical analysis of differential equations*. Cambridge University Press, Cambridge, 2009.
- [13] Gerd Leuchs and Thomas Beth. *Quantum information processing*. WILEY-VCH Verlag GmbH & Co.KGaA, Weinheim, 2003.

- [14] Stefan Kröll Mahmood Sabooni, Qian Li and Lars Rippe. *Efficient quantum memory using a weakly absorbing sample*. *PHYSICAL REVIEW LETTERS*, VOLUME 110, March 2013.
- [15] Leonard Mandel and Emil Wolf. *Optical coherence and quantum optics*. Cambridge University Press, Melbourne, 1995.
- [16] Hugues de Riedmatten Mikael Afzelius, Christoph Simon and Nicolas Gisin. *Multimode quantum memory based on atomic frequency combs*. May 2009.
- [17] Wolfgang Tittel Nicolas Gisin, Gregoire Ribordy and Hugo Zbinden. *Quantum Cryptography*. *REVIEWS OF MODERN PHYSICS*, VOLUME 74.
- [18] Lars Rippe. *Quantum computing with naturally trapped sub-nanometre-spaced ions*. PhD thesis, Lund university, 2006.
- [19] B.E.A. Saleh and M.C. Teich. *Fundamentals of photonics*. John Wiley & Sons, Inc., New Jersey, 2nd edition, 2007.
- [20] Anthony E. Siegman. *Lasers*. University Science Books, Mill Valley, 1986.
- [21] Axel Thuresson. *Numerical simulations of highly efficient quantum memories*. Master's thesis, Lund University.
- [22] Wikipedia. *Rotating wave approximation*. http://en.wikipedia.org/wiki/Rotating_wave_approximation, accessed 2014, last modified November 2013.
- [23] Wikipedia. *Slowly varying envelope approximation*. http://en.wikipedia.org/wiki/Slowly_varying_envelope_approximation, accessed 2014-01-28, last modified December 2013.
- [24] Wikipedia. *Bloch sphere*. http://en.wikipedia.org/wiki/Bloch_sphere, accessed 2014-01-28, last modified January 2014.
- [25] Wikipedia. *Fourier transform*. http://en.wikipedia.org/wiki/Fourier_transform, accessed 2014-01-28, last modified January 2014.
- [26] R.L Cone R.W Equall R.L Hutcheson Y. Sun, C.W Thiel. *Recent progress in developing new rare earth materials for hole burning and coherent transient applications*. *Journal of Luminescence*, VOLUME 98, july 2002.